Received: 17 June 2024 | Revised: 10 March 2025 | Accepted: 11 March 2025

DOI: 10.1002/cac2.70021

CANCER COMMUNICATIONS Open Access

ORIGINAL ARTICLE

Immunosuppressive JAG2$^+$ tumor-associated neutrophils hamper PD-1 blockade response in ovarian cancer by mediating the differentiation of effector regulatory T cells

Chenyang Wang[1] | **Moran Yang**[1,2] | **Yujing Zhong**[1] | **Kankan Cao**[1] | **Xueling Wang**[1] | **Chen Zhang**[1] | **Yiying Wang**[1] | **Mengdi He**[1] | **Jiaqi Lu**[1,2] | **Guodong Zhang**[2] | **Yan Huang**[3] | **Haiou Liu**[1]

[1]Shanghai Key Laboratory of Female Reproductive Endocrine Related Diseases, Obstetrics and Gynecology Hospital, Fudan University, Shanghai, P. R. China

[2]Department of Gynecologic Oncology, Obstetrics and Gynecology Hospital, Fudan University, Shanghai, P. R. China

[3]Department of Gynecologic Oncology, Shanghai Cancer Center, Fudan University, Shanghai, P. R. China

Correspondence
Haiou Liu, Shanghai Key Laboratory of Female Reproductive Endocrine Related Diseases, Obstetrics and Gynecology Hospital, Fudan University, Shanghai 200011, P. R. China.
Email: liuhaiou@fudan.edu.cn

Yan Huang, Department of Gynecologic Oncology, Shanghai Cancer Center, Fudan University, Shanghai 200032, P. R. China.

Abstract

Background: Tumor-associated neutrophils (TANs) play a critical role in modulating immune responses and exhibit significant heterogeneity. Our previous study demonstrated that jagged canonical Notch ligand 2 (JAG2)$^+$ TANs were associated with an immunosuppressive microenvironment in high-grade serous ovarian cancer (HGSOC), but the underlying mechanism remains unclear. This study aimed to elucidate the role of JAG2$^+$ TANs in tumor immunosuppressive microenvironment in HGSOC.

List of abbreviations: Blimp-1, B lymphocyte-induced maturation protein 1; CD103/ITGAE, Integrin alpha E; CFSE, Carboxyfluorescein succinimidyl ester; CI, Confidence interval; CPS, Combined positive score; CTLA4, Cytotoxic T-lymphocyte associated antigen 4; CXCL, C-X-C motif chemokine ligand; CXCR, C-X-C chemokine receptor; DEGs, Differentially expressed genes; eTregs, Effector regulatory T cells; FCM, Flow cytometry; FIGO, International federation of gynecology and obstetrics; FLOWSOM, Self-organizing maps of flow cytometry data; Foxp3, Forkhead box protein P3; GO, Gene ontology; GSEA, Gene set enrichment analysis; GSVA, Gene set variation analysis; GZMB, Granzyme B; HES1, Hairy and enhancer of split-1; HGSOC, High-grade serous ovarian cancer; HR, Hazard ratio; ICI, immune checkpoint inhibitor; ICOS, Inducible T-cell co-stimulator; IF, Immunofluorescence; IFN-γ, Interferon-gamma; IHC, Immunohistochemistry; IL-10, interleukin-10; JAG2, Jagged canonical notch ligand 2; KEGG, Kyoto Encyclopedia of Genes and Genomes; MFI, Mean Fluorescent Intensity; mIHC, Multiplex immunohistochemistry; NICD1, Notch1 intracellular domain; OS, Overall survival; PB, Peripheral blood; PBNs, Peripheral blood neutrophils; PD-1, Programmed cell death 1; PD-L1, programmed cell death ligand 1; PDTO, Patient-derived tumor organoids; qRT-PCR, Quantitative real-time polymerase chain reaction; RBPJ, Recombination signal binding protein for immunoglobulin kappa J region; scRNA-seq, Single-cell RNA sequencing; siRNA, Small interfering RNA; TANs, Tumor-associated neutrophils; TCF1, T Cell Transcription Factor 1; TCGA, The Cancer Genome Atlas; Teff, Effector T cell; Tex, Exhausted T cells; Tex-int, Intermediate-exhausted T cells; TFs, Transcription factors; TLS, Tertiary lymphoid structures; TMA, Tissue microarrays; TME, Tumor microenvironment; TNF-α, Tumor necrosis factor-α; Tpex, Progenitor-exhausted T cells; Tregs, Regulatory T cells; t-SNE, t-distributed stochastic neighbor embedding; UMAP, Uniform manifold approximation and projection.

Chenyang Wang and Moran Yang contributed equally.

Email: huangyan19790315@163.com

Guodong Zhang, Department of Gynecologic Oncology, Obstetrics and Gynecology Hospital, Fudan University, Shanghai 200011, P. R. China.
Email: gdzhang12@fudan.edu.cn

Funding information
National Natural Science Foundation of China, Grant/Award Numbers: 82072881, 82273205, 82203665, 82473274; Natural Science Foundation of Shanghai, Grant/Award Number: 23ZR1408300; Shanghai Science and Technology Innovation Action Plan, Grant/Award Numbers: 23Y11909500, 23Y11901800; Shanghai Clinical Research Center for Gynecological Diseases, Grant/Award Number: 22MC1940200

Methods: HGSOC samples were collected, with 274 samples constituting two independent cohorts (training and validation cohorts) and an additional 30 samples utilized to establish patient-derived tumor organoids (PDTOs). We characterized the number and phenotype of JAG2$^+$ TANs by multiplex immunohistochemistry, flow cytometry, and single-cell RNA sequencing (scRNA-seq). We investigated the biological functions of JAG2 in immune evasion using in vitro co-culture systems, flow cytometry, tumor-bearing mouse models, and PDTOs.

Results: JAG2$^+$ TANs expressed elevated levels of immunosuppressive molecules, including programmed cell death ligand 1 and CD14, and had independent prognostic value for the overall survival of patients with HGSOC. scRNA-seq analysis revealed that JAG2$^+$ TANs exhibited a terminally mature phenotype. The infiltration of JAG2$^+$ TANs was positively correlated with the abundance of effector regulatory T cells (eTregs). Interaction with JAG2$^+$ TANs skewed CD4$^+$ T cells towards an eTreg phenotype, a process that was suppressed by the Notch inhibitor LY3039478 and induced by recombinant Jagged2. Furthermore, we demonstrated that JAG2$^+$ TANs enhanced Notch signaling activation, ultimately promoting recombination signal binding protein for immunoglobulin kappa J region (RBPJ)-induced differentiation of naïve CD4$^+$ T cells into eTregs. Clinically, JAG2$^+$ TANs could serve as a biomarker for assessing immunotherapy resistance in various solid tumors. Pharmacological targeting of Notch signaling with LY3039478 or JAG2 neutralization antibodies enhanced the efficacy of programmed cell death protein 1 (PD-1) monoclonal antibodies (mAbs) in both xenograft and PDTO models.

Conclusions: The emergence of JAG2$^+$ TANs is crucial for the differentiation of eTregs, which triggers immune evasion and resistance to anti-PD-1 therapy. Inhibiting Notch signaling with LY3039478 or JAG2 neutralization antibodies may overcome this anti-PD-1 resistance in HGSOC.

KEYWORDS
effector regulatory T cells, high-grade serous ovarian cancer, Jagged2, programmed cell death 1, Tumor-associated neutrophils

1 | BACKGROUND

Neutrophils, as the most numerous myeloid cells, play a critical role in innate immunity by combating acute infections or inflammatory conditions. Within the tumor microenvironment (TME), tumor-associated neutrophils (TANs) display dual roles—supporting tumor progression and exerting anti-tumor activity [1]. These cells contribute to tumor-associated inflammation through mechanisms such as angiogenesis stimulation, extracellular matrix modification, facilitation of metastasis, and suppression of immune responses [2–4]. Nevertheless, TANs also harbor anti-tumor phenotypes, such as promoting interferon-related immunostimulatory effects [5] and enhancing antigen presentation [6]. Recent analyses have highlighted correlations between various TAN subsets and tumor prognosis. For instance, programmed cell death ligand 1 positive (PD-L1$^+$) TANs and chemokine (C-C motif) ligands 4 positive (CCL4$^+$) TANs were enriched in tumor tissues and associated with poor prognosis in liver cancer [7]. Similarly, basic helix-loop-helix family member E40 positive (BHLHE40$^+$) TANs were associated with unfavorable outcomes in patients with pancreatic ductal adenocarcinoma (PDAC) [8].

Numerous studies have investigated the evaluation of PD-L1 expression in ovarian cancer (OV), particularly its prognostic significance. A recent meta-analysis revealed that PD-L1 positivity in OV patients was associated with favorable OS when studies used a combined positive score (CPS) as a scoring method [9]. Another pooled analysis

showed that positive PD-L1 expression predicted a longer OS time in patients with high-grade serous ovarian cancer (HGSOC) [10]. However, elevated PD-L1 levels do not reliably predict the therapeutic efficacy of immune checkpoint inhibitors (ICI) therapies in patients with OV [11]. The identification of biomarkers capable of predicting therapeutic responses to ICIs warrants further investigation.

The infiltration of TANs affects the response to various anti-tumor treatments. Increased peripheral blood neutrophils and elevated neutrophil-to-lymphocyte ratios (NLR) are associated with deleterious outcomes in patients undergoing ICI therapy [1, 12, 13]. Conversely, TANs can express immune checkpoint ligands such as PD-L1 [14, 15] and may acquire an anti-tumor phenotype in response to immunotherapy [16]. Therefore, TANs represent both a target for and a mechanism of resistance to ICIs. Identifying the key molecule(s) involved in the diverse functions of TANs is crucial for selectively targeting TANs in tumor treatment. In our previous study, $JAG2^+$ TANs were associated with poor prognosis, and we have demonstrated the crosstalk between $JAG2^+$ TANs and immunosuppressive tumor microenvironment in ovarian cancer [17]. Moreover, treatment with the specific Notch inhibitor LY3039478 enhanced the cytotoxicity of $CD8^+$ T cells in ovarian cancer with high $JAG2^+$ TAN infiltration. Nevertheless, the molecular mechanisms by which $JAG2^+$ TANs exert their functions are still unclear.

Notch signaling is pivotal in determining early cell fate. In lymphocyte development, distinct Notch ligand-receptor combinations regulate lineage-specific differentiation. For example, delta-like ligand 4 (DLL4) binding to Notch1 directs thymic T cell lineage specification, while Notch2 activation facilitates dendritic cell subset differentiation within the intestinal lamina propria [18]. DLL-mediated Notch signaling favors the differentiation and effector functions of T helper cell 1 (Th1) cells, whereas Jagged ligands induce the differentiation of T helper cell 2 (Th2) and regulatory T (Treg) cells [19]. Tregs, defined by their unique immunosuppressive role, are distinguished by the expression of the transcription factor forkhead box protein P3 (Foxp3). Upon antigen stimulation, naïve Treg cells can be converted to highly suppressive effector Treg (eTreg) cells [20]. As the dominant Treg cell subpopulation in tumors, eTregs contribute to an immunosuppressive niche and limit the therapeutic success of immunotherapy in non-small cell lung cancer [21]. This subset is phenotypically marked by augmented expression of cytotoxic T-lymphocyte associated antigen 4 (CTLA4), interleukin-10 (IL-10), inducible T-cell co-stimulator (ICOS), and other markers [20]. Previous studies have shown that Notch1 cooperates with mothers against decapentaplegic homolog 3 (SMAD3) and recombination signal binding protein for immunoglobulin kappa J region (RBPJ) to activate *FOXP3* transcription [22]. Alternatively, the transcription factor interferon regulatory factor 4 (IRF4) plays a dominant role in eTreg differentiation by driving B lymphocyte-induced maturation protein 1 (Blimp-1) to induce IL-10 and ICOS expression [23]. The transcription factor c-avian musculoaponeurotic fibrosarcoma (c-Maf), upregulated by Notch pathway activation, synergizes with Blimp-1 to promote IL-10 expression in Th1 cells [24]. Nevertheless, whether Notch signaling regulates eTreg cells differentiation remains elusive.

To understand the mechanisms underpinning the protumorigenic functions of $JAG2^+$ TANs in HGSOC, we systematically interrogated the cellular sources of JAG2 in HGSOC. We identified TANs as the primary cellular source of JAG2. Through trajectory analysis and functional enrichment, we characterized the immunosuppressive features of $JAG2^+$ TANs. Furthermore, we discovered that $JAG2^+$ TANs mediate the differentiation of eTregs in a Notch1/RBPJ-dependent manner. In addition, the combination of a Notch inhibitor with anti-PD-1 produced synergistic antitumor effects. Overall, our study suggests that $JAG2^+$ TANs represent a promising therapeutic target for the selective depletion of tumor-infiltrating eTregs in cancer immunotherapy.

2 | MATERIALS AND METHODS

2.1 | Cell lines

Mouse ovarian cancer cell line OV2944-HM1 (HM1) was purchased from the RIKEN BioResource Research Center (Tsukuba, Ibaraki, Japan). Mouse ovarian cancer cell line ID8 was a gift from Dr. Chen Dong (Institute of Immunology, Tsinghua University, Beijing, P. R. China). From this, we developed a highly aggressive ID8agg subline through serial passage in wild-type hosts. To track tumor burden in intraperitoneal models, ID8agg cells were transfected with luciferase (Heyuan Biotech, Shanghai, P. R. China). Stable luciferase-expressing ID8agg (ID8agg-Luc) cells were isolated by limiting dilution following selection with puromycin. ID8agg and HM1 cells were cultured in high-glucose dulbecco's modified eagle medium (11965092, Gibco, FL, USA) or minimum essential medium α containing a pool of nucleosides (12571063, Gibco), respectively. Both media were supplemented with 10% fetal bovine serum (FBS, F8318, Sigma, MO, USA), 100 U/mL penicillin-streptomycin (15140122, Invitrogen, Carlsbad, CA, USA), and cultured at 37°C in a humidified incubator with 5% CO_2. All cell lines used in this study were tested to confirm they were free of mycoplasma and were authenticated by short-tandem repeat analysis.

2.2 | Mice and in vivo experiments

B6C3F1 mice (4-6 weeks old, female) were purchased from Charles River Laboratories (Beijing, China). C57/BL6 mice (4-6 weeks old, female) were purchased from Shanghai Jiesijie Laboratory Animal Co., Ltd. (Shanghai, P. R. China). For subcutaneous isograft models, B6C3F1 mice were randomly assigned to four groups ($n = 6$). Each mouse received a 100 μL injection of a single-cell suspension containing 1×10^6 HM1 cells in ice-cold phosphate-buffered saline (PBS) into the right flank using a 27G needle under anesthesia. Tumor growth was monitored daily and measured every two days using the formula: $V = \text{length} \times \text{width}^2 \times 0.5$ (mm^3). For intraperitoneal isograft models, C57/BL6 mice were randomly assigned to four groups ($n = 6$). Each mouse received a 100 μL injection of a single-cell suspension comprising 1×10^7 ID8agg-Luc cells in ice-cold PBS into the abdominal cavity using a 27G needle. Mice were then treated with intraperitoneal injections of 200 μg of anti-PD-1 antibody (BE0033, BioXCell, West Lebanon, NH, USA) per mouse, or a mouse IgG1 isotype control (BE0083, BioXCell), or 8 mg/kg LY3039478 (S7169, Selleckchem, Houston, TX, USA) by oral gavage formulated in 1% Na-CMC (200 μL, 9004-32-4, Sangon Biotech, Shanghai, P. R. China), or a combination of anti-PD-1 and LY3039478. Intraperitoneal injections were administered on day 3 and every third day until the end of the experiment. For neutralizing Jagged2, C57/BL6 mice received intraperitoneal injections of 250 μg anti-Jagged2 (BE0125, BioXCell, West Lebanon, NH, USA), or a mouse IgG1 isotype control (BE0083, BioXCell) on days 4, 6, 8, 10, 12, 14, 16, and 18 following the injection of ID8agg-luc cells. For survival analysis, mice were considered "dead" when they reached a moribund state (minimal mobility) and were euthanized by carbon dioxide inhalation for humane concerns. All animals were housed in the Laboratory Animal Center of Fudan University, which met specific pathogen-free standards. The handling of animals was conducted in strict accordance with the Principles for the Utilization and Care of Vertebrate Animals and the Guide for the Care and Use of Laboratory Animals. Animal experiments were approved by the Ethics Committee of the Department of Laboratory Animal Science of Fudan University (2022JSFCKYY-063).

2.3 | Bioluminescence imaging

Mice were intraperitoneally injected with 150 mg/kg D-Luciferin, potassium salt (40902ES03, Yeasen, Shanghai, P. R. China) in Dulbecco's phosphate-buffered saline (DPBS), and images were acquired 15 min later. Mice were then scanned using an in vivo Imaging System (IVIS) (Bruker-FX Pro, MA, USA), with imaging performed using the Living Image software (Bruker MISE, version 7.2.0). Quantification of bioluminescence signals was performed with Living Image software, analyzing photon flux (photons per second) in defined regions of interest (ROIs).

2.4 | Clinical tissue samples

The training cohort consisted of 120 patients with HGSOC who underwent surgical resection at the Gynecology and Obstetrics Hospital of Fudan University from March 2013 to November 2015. The validation cohort comprised 154 patients with HGSOC from the Fudan University Shanghai Cancer Center from January 2012 to October 2019. Fresh tumor tissues from 60 patients with HGSOC at Fudan University Shanghai Cancer Center were used for flow cytometry (FCM) analysis ($n = 30$) and ex vivo ($n = 30$) intervention. None of the patients had an autoimmune disorder or received chemotherapy prior to tumor resection. All HGSOC specimens were surgically resected from the primary site and histologically verified. Patient clinicopathological characteristics are detailed in Supplementary Table S1. Pathological staging and histological types were determined according to the International Federation of Gynecology and Obstetrics (FIGO) classification (2018 edition). Overall survival (OS) was calculated from the date of surgery to the last follow-up or death. The training cohort was followed up until March 2019, while the validation cohort was followed up until September 2023. PB samples were collected from eight healthy donors. The study was approved by the Ethics Committee of Obstetrics and Gynecology Hospital, Fudan University (Kyy2016-49, Kyy2017-27) and the Ethics Committee of the Fudan University Shanghai Cancer Center (050432-4-2108*). All procedures were performed according to the Declaration of Helsinki, and written informed consent was obtained from participants.

2.5 | Immunohistochemistry (IHC) and evaluation of immunostaining

The protocol for constructing tissue microarrays (TMAs) and performing IHC staining has been detailed in our previous study [25]. Details of the primary antibodies are provided in Supplementary Table S2. Dual staining was conducted with horseradish peroxidase (HRP) and alkaline phosphatase (AP) polymer systems (Vector Laboratories, Newark, CA, USA), following the manufacturer's protocols. TMA sections were scanned with the KF-PRO-120 digital slide scanner (KFBIO Technology, Zhejiang,

China) and evaluated independently by two investigators who were blinded to the clinicopathological data. Positive cells were counted from two tissue cores, and an average density (number of positive cells per mm^2) was adopted. The proportion of PD-L1 positive tumor cells was reported as the combined positive score (CPS), calculated as $\text{CPS} = \frac{\text{PD-L1}^+ \text{ tumor-associated immune cells} + \text{PD-L1}^+ \text{ tumor cells}}{\text{Total tumor cells}} \times 100$. A minimum of 100 cells were assessed. Any membrane-based positivity in tumor cells was considered positive. For CPS, PD-L1 positivity was defined as ≥1. The minimal *P* value method provided by the X-tile software (version 3.6.1, Yale University, New Haven, CT, USA) was used to automatically find the cutoff values of low- and high-density groups for JAG2 and CD66b, ICOS, and FOXP3 double-positive cells.

2.6 | Multiplex immunohistochemistry (mIHC)

mIHC was performed using an Opal 5-color IHC kit (YB007, YOBIBIO Biosciences, Shanghai, P. R. China). Paraffin-embedded slides were first baked, followed by dewaxing and rehydration. Antigen retrieval was then performed with a citrate buffer (pH = 6.0). The slides were then blocked in a blocking buffer for 10 min and sequentially incubated with primary antibodies and horseradish peroxidase (HRP)-conjugated secondary antibodies. Following this, the slides were stained with tyrosine signal amplification (TSA) to label the antigens. This staining procedure was repeated for all four antigen markers. Primary antibodies used included anti-JAG2 (dilution 1:200, HPA030636, Sigma), CD66b (dilution 1:200, 392902, Biolegend), FOXP3 (dilution 1:500, 320201, Biolegend), and ICOS (dilution 1:200, Biolegend). The dyes Opal520, Opal570, Opal620, Opal690, and 4'6-diamidino-2-phenylinodole (DAPI, Sigma-Aldrich, St. Louis, MO, USA) were employed for staining. Finally, sample imaging was conducted with the KF-FL-020 digital slide scanner (KFBIO Technology). Spatial proximity analyses between $ICOS^+$ Tregs/$ICOS^-$ Tregs and $JAG2^+$ TANs were performed using multiplex immunofluorescence in tissue sections from six HGSOC patients. Two representative fields per sample were imaged at 100× magnification. Maximum intensity projection images were reconstructed in CaseViewer (Version 2.4, 3DHISTECH, Budapest, Hungary) and exported to ImageJ (Version 1.45, NY, USA) for quantitative spatial analysis. The XY location of objects and fluorescence colocalization of ICOS staining in Treg objects were determined using ImageJ software. The distance from $ICOS^+$ Treg or $ICOS^-$ Treg cells to the nearest $JAG2^+$ TANs was calculated.

2.7 | Immunofluorescence (IF)

A total of 7×10^3 cells were prepared in 100 μL complete RPMI-1640 and concentrated on the slide using a cytospin at 600 rpm for 5 min. The cells were then fixed with 1% formaldehyde for 20 min. The samples were covered with the primary antibody, including anti-cleaved Notch1 (4147T, Cell Signaling Technology, Danvers, MA, USA) and anti- hairy and enhancer of split-1 (anti-HES1, ab108937, Abcam, Cambridge, MA, USA) and incubated at 4°C overnight. The next day, the samples were incubated with a secondary antibody (Alexa Fluor 488-conjugated Donkey anti-Rabbit IgG, 711-545-152, Jackson Immunoresearch Laboratories, West Grove, PA, USA) at room temperature for 1 hour. Following PBS washes, nuclei were stained with DAPI (Sigma-Aldrich) for 10 minutes. Slides were coverslipped and visualized under the Leica Thunder imaging system (DM6 B, Wetzlar, Germany) for image acquisition.

2.8 | Flow cytometry

Tissues were collected in ice-cold PBS. Blood samples sourced from eight healthy donors at the Gynecology and Obstetrics Hospital of Fudan University were also collected in potassium/EDTA-coated tubes, and erythrocytes were lysed using RBC lysis buffer for 10 min. Fresh tissue from mouse and human tumors was collected, digested with a Gentle MACS Dissociator (Miltenyi, Bergisch Gladbach, Germany), and then passed through a Falcon 70-μm cell strainer. After washing with PBS, red blood cells were lysed, and the samples were incubated with the Zombie Aqua™ Fixable Viability Kit (423102, Biolegend, San Diego, CA, USA) prior to staining. Single-cell suspensions were then stained with a panel of fluorochrome-tagged monoclonal antibodies (Supplementary Table S3). For intracellular staining, cells were permeabilized in 100 μL of Fixation solution (420801, Biolegend) for 40 min at 4°C, washed with 1× Perm/Wash buffer (421002, Biolegend), and resuspended in the indicated antibodies diluted in 1 mL of 1× Perm/Wash buffer for 30 min at 4°C. Isotype-matched antibody-stained samples were used as negative controls. For sample acquisition, a Beckman Coulter CytoFlEX flow cytometer (Beckman Coulter, Miami, FL, USA) with FACS CytExpert software was used. Data analysis, including quantification and visualization, was performed using FlowJo Software (version 10.8.1, BD BioSciences, San Jose, CA, USA). The FlowSOM 3.0.18 plugin and t-SNE were employed to analyze Treg cell populations from the concatenated dataset.

2.9 | Uniform manifold approximation and projection (UMAP) and trajectory analysis of neutrophils

The manually gated neutrophils FCM population was exported as a separate FCS file. Variables with low variance (cells with the same expression value of all markers) were removed, and the data were transformed using asinh(x) with the R package scDataviz (https://github.com/kevinblighe/scDataviz). Normalization was carried out by size factor through principal component analysis. Unsupervised clustering was conducted using the Leiden community detection method with the number of nearest neighbors (k) set to 100. Trajectory analysis was performed using the slingshot R package [26] (https://github.com/kstreet13/slingshot), with Cluster 4 selected as the origin. Multiple disjoint trajectories were allowed by setting the omega parameter to TRUE.

2.10 | Preparation of tumor-conditioned medium (TCM)

HGSOC tumor tissues were washed with PBS and minced in RPMI-1640 medium containing 3% FBS, 10 mM HEPES (15630080, Gibco, Grand Island, NY, USA), and 100 μg/mL penicillin-streptomycin (15140122, Invitrogen). After 24 hours, the medium was harvested, centrifuged at 500 ×*g* for 10 min to remove cellular debris, and filter-sterilized using SteriFlip vacuum filters (Merck, Billerica, MA, USA). TCM was then aliquoted and stored at -80°C until use.

2.11 | Purification of human neutrophils

Human peripheral blood neutrophils (PBNs) sourced from eight healthy donors at the Gynecology and Obstetrics Hospital of Fudan University were isolated using Polymorphprep (Axis-Shield, 1114683, Dundee, UK). Following centrifugation (500 ×*g*, 30 minutes, 20 ± 2°C), the neutrophil-rich pellet was harvested. Purification was achieved by washing the pellet with serum-free RPMI-1640 medium, followed by centrifugation at 400 ×*g* for 10 minutes. The purified neutrophils were cultured with 50% TCM for 24 h. Fluorescence-activated cell sorting (FACS)-sorting of $JAG2^{+/-}$ TANs was performed using a BD FACS Aria III cell sorter with BD FACS Diva 9.0/1 software (BD Biosciences, San Jose, CA, USA). PE-conjugated anti-human JAG2 antibody (dilution: 1:50, 346904, Biolegend) was used for the isolation of $JAG2^{+}$ TANs. Non-fluorescent samples were included as negative controls to establish baseline fluorescence thresholds. Sorted cells were collected and centrifuged, and the pellets were used for co-culture. For tumor samples, tumor samples were dissected into small pieces with a diameter <1 mm, and dissociated using Collagenase IV (V900893, Sigma) in RPMI 1640 for 40 min. The resulting cells were filtered through a 400 mm filter and washed with DPBS (500 ×*g* and 10 min). The cell suspension was then stained with and sorted using FCM (BD FACS Aria III).

2.12 | Magnetically-activated cell sorting (MACS)

Peripheral blood mononuclear cells (PBMCs) whole blood by density gradient centrifugation with Lymphoprep (Axis-Shield, Oslo, Norway) at 800 ×*g* for 20 minutes. Cells at the interface layer were harvested and subjected to two PBS washes. Positive selection of monocytes was performed using MACS with $CD4^{+}$ microbeads (130-045-101, Miltenyi, Bergisch Gladbach, Germany) or $CD8^{+}$ microbeads (130-045-201, Miltenyi), following the manufacturer's instructions.

2.13 | Co-culture experiments

For in vitro co-culture of $JAG2^{+}$ TANs with naïve $CD4^{+}$ T cells, $JAG2^{+/-}$ TANs were mixed in a 1:1 ratio with $CD4^{+}$ T cells, and we plated 4×10^{4} cells of the mixture in a U-bottom 96-well plate with 100 μL RPMI-1640 medium containing 10% FBS per well. The mixed cells were continuously cultured for 72 h with anti-CD3/CD28 activation beads (11452D, Thermo Fisher Scientific, Waltham, MA, USA) at a 1:2 bead-to-cell ratio, in the presence of 30 U/mL of IL-2 (589104, Biolegend), 5 ng/mL transforming growth factor beta 1 (TGF-β1, 781802, Biolegend), 3 μg/mL anti-IL-4 (500838, Biolegend), 3 μg/mL anti-interferon-gamma (anti-IFN-γ, 506532, Biolegend), with or without 1 μmol/L LY3039478, to induce Treg cell differentiation.

2.14 | T cell proliferation assays

$CD8^{+}$ T cells were isolated from peripheral blood mononuclear cells using MACS human $CD8^{+}$ microbeads, achieving a purity of 97% as determined by flow cytometry. For carboxyfluorescein succinimidyl ester (CFSE) proliferation assays, 1×10^{5} isolated human $CD8^{+}$ T cells were labeled with 5 μmol/L CFSE (423801, Biolegend). The labeled cells were then incubated with anti-CD3/CD28 beads (ThermoFisher Scientific) at a 1:1 bead-to-cell ratio in RPMI-1640 medium with 30 U/mL rhIL-2 (Biolegend). Proliferation was analyzed by FCM on day 3.

2.15 | T cell cytokine assays

For intracellular cytokine staining, 1×10^5 isolated $CD8^+$ T cells were incubated with anti-CD3/CD28 beads at a 1:1 ratio in RPMI-1640 medium with 30 U/mL rhIL-2 for 3 days. The cells were then incubated with 1× Brefeldin A Solution (420601, Biolegend) for 4-6 h before immunostaining. Cells were processed with Fixation/Permeabilization Buffer (424401, Biolegend) according to the manufacturer's instructions. The permeabilized cells were subsequently stained with anti-IFN-γ (506538, BioLegend).

2.16 | In vitro T cell suppression assays

For the suppression assay of $JAG2^+$ TANs, 1×10^5 CFSE-stained $CD8^+$ T cells were co-cultured with purified $JAG2^{+/-}$ TANs at a 1:1 ratio in 96-well U-bottom plates with RPMI-1640 medium containing 10% FCS. For the suppression assay of eTregs, differentiated Treg cells were purified using MACS with $CD25^+$ microbeads (130-092-983, Miltenyi). 1×10^5 CFSE-stained $CD8^+$ T cells were co-cultured with purified differentiated Tregs at a 1:1 ratio in 96-well U-bottom plates with RPMI-1640 containing 10% FCS. On day 3, cells were collected and stained with an anti-human CD8 antibody (344710, Biolegend). T cell proliferation and cytokine production were subsequently assessed via FCM.

2.17 | RNA extraction and quantitative real-time polymerase chain reaction (qRT-PCR)

Total RNA was isolated using the EZ-press RNA Purification Kit (B0004DP, EZBioscience, Shanghai, P. R. China), followed by reverse transcription into cDNA with a synthesis kit (11120ES60, Yeasen). The RNA quantity and concentration were determined using a spectrophotometer. qRT-PCR was conducted using the SYBR Green Master Mix Kit (11202ES08, Yeasen) in accordance with the manufacturer's instructions. The 10 μL PCR reaction system comprised 10% cDNA template, 10% gene-specific primer pairs, 50% SYBR Green master mix, and 30% nuclease-free water. PCR amplification was performed with an initial 5-min denaturation at 95°C, followed by 38 cycles of 95°C for 10 seconds, 57°C for 25 seconds, and 72°C for 20 seconds for denaturation, annealing, and extension, respectively. The specific primers used for qRT-PCR are listed in Supplementary Table S4. Each assay was conducted in triplicate. GAPDH served as the internal reference, and the data were analyzed using the $2^{-\Delta\Delta CT}$ method.

2.18 | RNA interference

Small interfering RNAs (siRNAs) duplexes were purchased from Genomeditech Co., Ltd. (Shanghai, P. R. China), and their sequences are provided in Supplementary Table S5. The siRNA targeting human *RBPJ* (GenBank accession no. NM_005349) was indicated as si*RBPJ*. The negative control siRNA (siControl) was nonhomologous to any human genome sequences. $CD4^+$ T cells (1×10^5) were seeded per well in a 6-well plate and transfected with 400 nmol/L siRNA using Lipofectamine™ 3000 Transfection Reagent (L3000001, Invitrogen) according to the manufacturer's instructions. The medium was replaced the next day, and cells were analyzed 3 days after transfection.

2.19 | Download and analysis of publicly available datasets

For immunotherapy datasets: In this study, five bulk RNA-seq datasets treated with immunotherapy were collected for analysis. The bulk RNA-seq and corresponding clinical data were obtained from public paper [27], the Gene Expression Omnibus (GEO) database (accession IDs: GSE91061, GSE78220, GSE93157), and the European Genome-phenome Archive database (accession ID: EGAS0001002556). To validate the predictive role of $JAG2^+$ TANs in the efficacy of ICI, we utilized the CheckMate 025 clinical trial cohort, for which RNA-seq data and corresponding clinical data are available from a previously published study [27, 28] To define the responders and non-responders, we aimed to faithfully use the criteria defined in the original clinical trials as much as possible. For the cohorts where Response Evaluation Criteria in Solid Tumors version 1.1 (RECIST v1.1) information is available, we used complete response (CR) and partial response (PR) as responders, and stable disease (SD) and progressive disease (PD) as non-responders. Publicly available single-cell RNA sequencing (scRNA-seq) data of HGSOC were obtained from the GEO database with accession IDs GSE137540 (peripheral blood) and GSE180661 (HGSOC tumor tissues). Transcriptomic and clinical data from project TCGA-OV in The Cancer Genome Atlas database were downloaded from the GDC Data Portal in December 2019. RNA-seq data were normalized to transcripts per million (TPM).

2.20 | Analysis of scRNA-seq

A standard Seurat workflow was used for the analysis of scRNA-seq data. Genes detected in fewer than three

cells were filtered out during quality control to ensure data reliability. Cells expressing less than 30% of mitochondrial transcripts were included for further analysis. After data normalization, principal component analysis, and UMAP, cell clusters were identified. For the identification of immune cell clusters, we use lineage-specific cell markers to distinguish cells [29, 30]. Differentially expressed genes (DEGs) were identified using the "limma" R package, with false discovery rate (FDR) correction for multiple comparisons. DEGs were defined as genes with adjusted P value < 0.05 and absolute log2 (fold change) > 0.25. The gene sets used in gene set enrichment analysis (GSEA) were obtained from the MSigDB (https://www.gsea-msigdb.org/gsea/msigdb). The JAG2$^+$ TAN feature gene set includes the top 16 genes with adjusted P value $< 1 \times 10^{-15}$ and log2 (fold change) > 1. The eTreg feature gene set includes the top 20 genes with adjusted P value $<$ 0.05 and log2 (fold change) > 0.25.

2.21 | Meta-analysis

A meta-analysis was conducted to investigate the association between JAG2$^+$ TANs and overall survival in HGSOC patients. Data from 13 independent HGSOC cohorts were collected from TCGA-OV, Array Express Archive (https://www.ebi.ac.uk/biostudies/arrayexpress) with the accession number: E-MATB-1733, and GEO databases (accession IDs: GSE8841, GSE8842, GSE9899, GSE14764, GSE18520, GSE19829, GSE26712, GSE30161, GSE32063, GSE49997, GSE51088). gene set variation analysis (GSVA, https://github.com/rcastelo/GSVA/) was applied to assess JAG2$^+$ TAN infiltration levels in each cohort, followed by patient stratification using the minimal P-value method provided by the X-tile software. HR of JAG2$^+$ TANs for OS as well as corresponding 95% confident interval (CI) were used for aggregation of survival results. The Q test was employed to assess heterogeneity, with the null hypothesis that all studies share identical effects. Additionally, the I squared (I^2) statistic was used to quantify heterogeneity in percentage terms and evaluate the consistency of data across the selected studies. The common effect model was selected as the summary effect model for the analysis.

2.22 | Deconvolution using cell-type identification by estimating relative subsets of RNA transcripts

Deconvolution was conducted using CIBERSORTx [31]. scRNA-seq data [30] was used to generate a single-cell reference sample matrix. This reference sample matrix was then used to generate a signature matrix using the default CIBERSORTx settings. Normalized gene expression data (TCGA-OV) were inputted to the CIBERSORTx Web site (https://cibersortx.stanford.edu/).

2.23 | GSVA for CD4$^+$ T cell subpopulations

The Magnuson signature score was computed using the GSVA package. The gene set of Magnuson signature can be obtained from online paper [32].

2.24 | Gene Ontology (GO) enrichment analysis of effector Tregs

We conducted GO annotation of the genes using the "clusterProfiler" R package, applying a significance threshold of P value < 0.05. The gene sets analyzed were obtained from the MSigDB database (https://www.gsea-msigdb.org/gsea/msigdb).

2.25 | Pseudotime analysis and trajectory inference of CD4$^+$ T cells

To determine the potential lineage differentiation among diverse CD4$^+$ T cell subpopulations, we performed trajectory analyses using Monocle2 (http://cole-trapnell-lab.github.io/monocle-release/). Naïve CD4$^+$ T cells were selected as the origin.

2.26 | Cell-to-cell communication of scRNA-seq data

To assess which ligand-receptor interactions potentially contribute to the transcriptomic changes in focal cell clusters, we applied NicheNet (https://github.com/saeyslab/nichenetr). Genes expressed with at least 0.1% target cells were kept for background expressed genes. To prioritize highly active ligands in sender cell populations, we employed Pearson correlation analyses, which assess the ability of ligands expressed by the sender cluster to predict changes in gene expression within the receiver cells.

2.27 | Transcription factors (TFs) analysis

We conducted single-cell regulatory network inference and clustering (SCENIC) analysis to forecast single-cell gene regulatory networks by following the standard workflow [33]. The raw count expression matrix

was imported into GENIE3 (https://github.com/aertslab/GENIE3) to build the initial co-expression gene regulatory networks (GRN). The regulon data were then analyzed based on TF motifs from hg19-tss-centered-10 kb (for human) database by RcisTarget (https://resources.aertslab.org/cistarget/). The regulon activity scores for individual cells were determined using AUCell (https://github.com/aertslab/AUCell).

2.28 | Short-term organoids culture and ex vivo intervention experiments

To faithfully recapitulate the tumor from its original derivation and assess its sensitivity to anti-PD-1 blockade, we developed a short-term organoids culture system for HGSOC, as previously described [25]. Briefly, fresh HGSOC tissues were minced into 1-2 cubic millimeter pieces and resuspended in DMEM with 10% FBS, 1% Pen/Strep, and 30 ng/mL rIL-2 (589102, Biolegend) mixed with 15% Matrigel (356234; Corning). This suspension was then plated at 40 μL per well in 48-well plates and incubated at 37°C to allow the cells to settle. The cultures were treated with 10 μg/mL anti-PD-1 antibody (329957, Biolegend), or 1 μmol/L LY3039478 in 1 mL DMEM for 2 days. An IgG2a isotype control (BE0085; BioXcell) was used as the negative control. For FCM analysis, a protein transporter inhibitor (Invitrogen, Carlsbad, CA, USA) was added to the media at a concentration of 1:500 for at least 4-6 hours before analysis.

2.29 | Unsupervised clustering of thirty organotypic tumor spheroids of HGSOC

Hierarchical clustering was conducted using the frequency of $CD45^+$ lymphocyte populations, effector molecules in $Foxp3^-CD4^+$ T cells and $CD8^+$ T cells, and apoptotic tumor cells. All cell frequencies are normalized to totals, log-transformed, and then z-transformed. Samples were clustered using complete linkage and Euclidean distance. Unsupervised hierarchical clustering identified two groups, responder and non-responder.

2.30 | Statistical analyses

Statistical analyses were performed using Prism software (version 8.0.1, GraphPad). For comparing means between two groups with normal or approximately normal distributions, unpaired *t*-tests were applied. For datasets that did not meet the Shapiro-Wilk normality test, Mann-Whitney U tests were applied for unpaired datasets, and paired *t*-tests were applied for paired datasets. When comparing three or more groups, a one-way analysis of variance (ANOVA) with multiple comparison corrections (Turkey's test) was applied. Chi-square tests were used to compare categorical variables between independent groups. Significant correlations between two variables were assessed using Spearman's correlation coefficient. In vivo experiments, significance was determined by two-way ANOVA (considering time and treatment) with Sidak's multiple comparison test. For the ex vivo assay, significance was evaluated using the Friedman test with Dunn's multiple comparison test. Kaplan-Meier plots for survival comparison were analyzed using the log-rank test between groups. Specific statistical methods are indicated in the figure legends. *P* values are presented directly and with numerical values or asterisks ($*P < 0.05$, $**P < 0.01$, and $***P < 0.001$). Data are expressed as mean ± standard deviation (SD).

3 | RESULTS

3.1 | $JAG2^+$ TANs are terminally differentiated and serve as an independent survival predictor in HGSOC

To illustrate the specific role of $JAG2^+$ TANs in HGSOC, we investigated the cellular expression of JAG2 in the TME using FCM (Supplementary Figure S1A). JAG2 was found to be predominantly and highly expressed in neutrophils (Figure 1A-B). TANs have traditionally been considered mature and terminally differentiated cells [6]. However, the diversity in their maturation states remains unclear. The phenotypic transition of PBNs to TANs was further confirmed through the slingshot algorithm. Two trajectories, starting from cluster 4 and branching into cluster 3 and cluster 6, were constructed among 9 clusters identified by unsupervised clustering analysis (Figure 1C). Based on the expression of JAG2, maturity markers (CD11b, C-X-C chemokine receptor 4 [CXCR4]) [34, 35] and immunosuppression markers (CD14, PD-L1) [7, 36] in clusters 1-9, we identified three distinct neutrophil states within the blood and tumor microenvironment: immature, transitional, and mature. The immature state (clusters 1, 4, 8, and 9) was characterized by high expression of early circulation neutrophil markers [37], such as CD62L and C-X-C chemokine receptor 2 (CXCR2). Clusters 2, 5, and 7, with intermediate expression levels of several markers, including JAG2, were considered transitional states. The mature state (clusters 3, 6) was defined by either high JAG2, CD14, CXCR4, and PD-L1 expression (cluster 6) or the absence of JAG2 but high CXCR2 expression (cluster 3) (Figure 1D-E). Together, these data indicated that $JAG2^+$ TANs with high CD14,

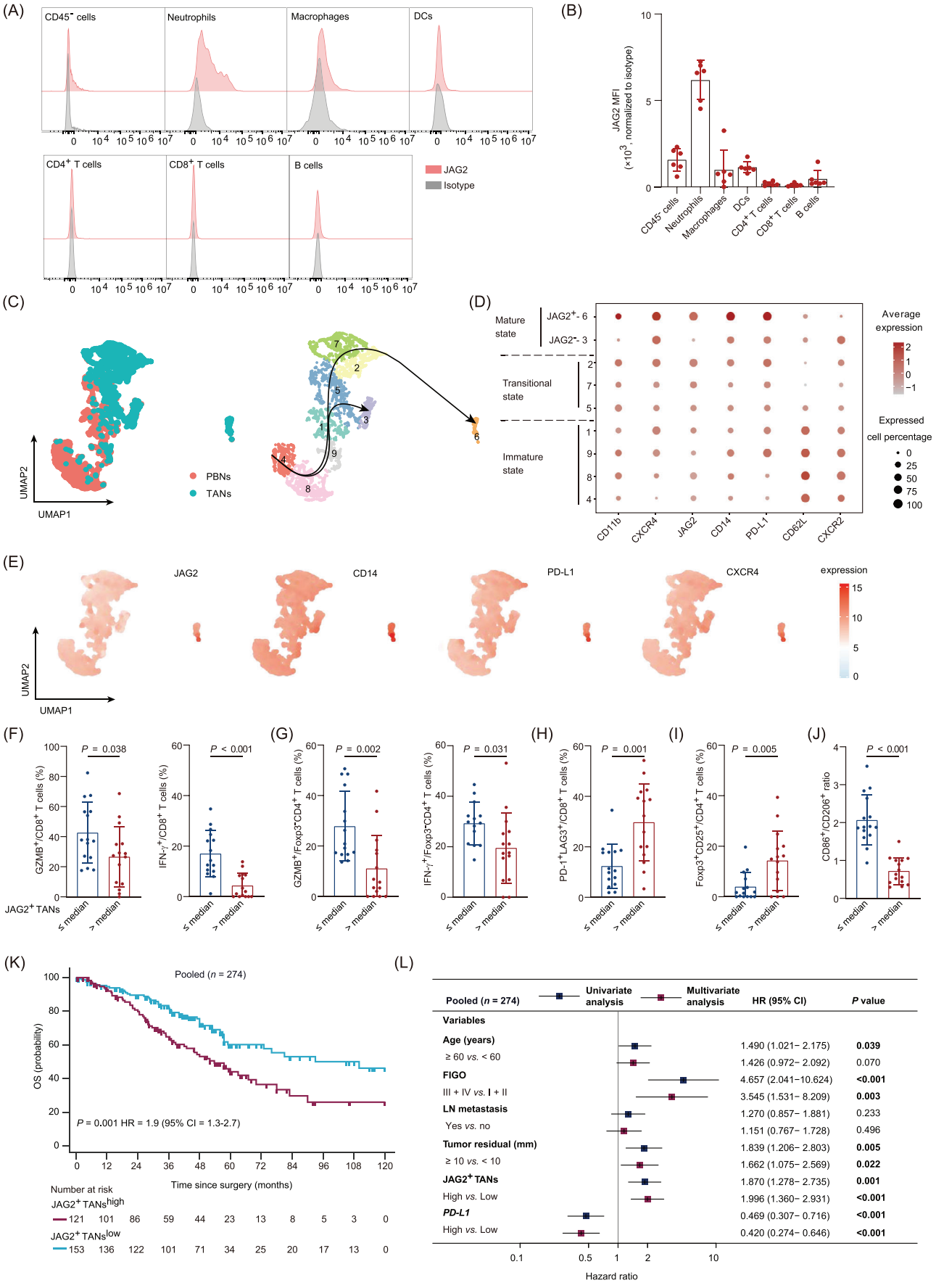

CXCR4, and PD-L1 expression are terminally mature neutrophils. We investigated the role of JAG2$^+$ TANs in the tumor immune microenvironment of HGSOC and found that the cytotoxic ability of CD8$^+$ T and conventional Foxp3$^-$CD4$^+$ T cells was significantly diminished in the JAG2$^+$ TANs^{high} subgroup, which was evidenced by the downregulation of effector molecules such as granzyme B (GZMB) and interferon-gamma (IFN-γ) compared to the JAG2$^+$ TANs^{low} subgroup (Figure 1F-G). Additionally, the proportion of PD-1$^+$LAG3$^+$CD8$^+$ T cells was increased in the JAG2$^+$ TANs^{high} subgroup (Figure 1H). Furthermore, higher levels of Treg (Foxp3$^+$CD25$^+$CD4$^+$) cells (Figure 1I) and a lower ratio of M1/M2 polarized macrophages (Figure 1J) were observed in the JAG2$^+$ TANs^{high} subgroup.

To explore the association between neutrophil subsets and patient survival, we separately categorized the patients from two independent cohorts into two groups on the basis of the IHC score of JAG2$^+$ TANs (Supplementary Figure S1B). The two independent cohorts were combined into a pooled dataset to minimize selection bias. Survival analysis confirmed poor survival outcomes for patients with high JAG2$^+$ TAN infiltration in each independent cohort as well as in the pooled dataset (Figure 1K, Supplementary Figure S1C-D). Univariate and multivariate Cox regression analyses indicated that JAG2$^+$ TAN infiltration could serve as an independent prognostic factor of OS in each independent cohort (training cohort: hazard ratio [HR] = 1.904, 95% confidence interval [CI] = 1.135-3.195, $P = 0.015$; validation cohort: HR = 2.419, 95% CI = 1.327-4.410, $P = 0.004$) (Supplementary Figure S1E-F) and in the pooled dataset (HR = 1.996, 95% CI = 1.360-2.931, $P < 0.001$) (Figure 1L).

3.2 | scRNA-seq results confirmed the immunosuppressive features of JAG2$^+$ TANs

To further decode the transcriptional signature of JAG2$^+$ TANs, we analyzed tumor-infiltrated myeloid cells using scRNA-seq data (GSE180661). We identified five myeloid cell subsets (Supplementary Figure S2A-B) and JAG2 was highly expressed in neutrophils (Supplementary Figure S2C).

Subsequently, we integrated scRNA-seq data from HGSOC tumor tissues (GSE180661) and peripheral blood (GSE137540) to dissect the landscapes of neutrophil states that could be differentially ascribed to tumors or blood (Figure 2A). We observed seven distinct states, characterized by the expression of ARG1$^+$, mitochondrially encoded NADH dehydrogenase 5 and mitochondrially encoded NADH dehydrogenase 2 (MT-ND5$^+$MT-ND2$^+$), CXCR2$^+$, interferon induced protein with tetratricopeptide repeats 1 and interferon-stimulated 15 kDa protein (IFIT1$^+$ISG15$^+$), S100 calcium binding protein A12 (S100A12$^+$), Fc fragment of IgG receptor IIIa and interferon-gamma receptor 1 (FCGR3A$^+$IFNGR1$^+$), and CD14$^+$JAG2$^+$ neutrophils (Figure 2B). According to the biological functions of neutrophils in these states confirmed by previous studies, we identified clusters potentially representing immunosuppression (CD14$^+$JAG2$^+$) [17, 38], as well as clusters associated with inflammatory response (S100A12$^+$)[39], specific chemotaxis (CXCR2$^+$) [6], arginine metabolism (ARG1$^+$) [6], oxidative phosphorylation (MT-ND5$^+$MT-ND2$^+$) [40], interferon response (IFIT1$^+$ISG15$^+$) [29] and IFN-γ response (FCGR3A$^+$IFNGR1$^+$) [7]. Some subsets in our data were consistent with reported neutrophil

FIGURE 1 JAG2$^+$ TANs endowed with a terminal differentiated phenotype serve as an independent survival predictor in patients with HGSOC. (A-B) Representative flow cytometry histograms (A) and statistical analysis (B; $n = 6$) displayed the expression of JAG2 in tumor and immune cell subpopulations within tumor tissue. (C) UMAP of neutrophils displayed nine subtypes. Each dot represents a single cell, color-coded by cell origins (left) and cell clusters (right). Slingshot on UMAP of neutrophils yielded 2 trajectories (black line with an arrow). (D) Cell phenotype-specific expression of marker genes for manually annotated clusters. Dot size denotes the expressed cell percentage. The color scale represents average gene expression. (E) Expression of selected immunosuppressive and mature markers in UMAP as shown in (C). The color indicates log-normalized gene expression. (F-J) Flow cytometric analysis was performed to evaluate the frequency of GZMB$^+$ and IFN-γ^+ cells in CD8$^+$ T cells (F), the frequency of GZMB$^+$ and IFN-γ^+ cells in Foxp3$^-$CD4$^+$ T cells (G), the frequency of PD-1$^+$LAG3$^+$ cells in CD8$^+$ T cells (H), the frequency of Foxp3$^+$CD25$^+$ cells in CD4$^+$ T cells (I), and the ratio of CD86$^+$ to CD206$^+$ cells in CD68$^+$ cells (J) in primary HGSOC tumors. Tumors were stratified into high and low JAG2$^+$ TAN infiltration based on the median cutoff value ($n = 30$). Data are presented as mean ± standard deviation, and statistical significance was determined using an unpaired two-tailed t-test. (K) Kaplan-Meier curve for overall survival of patients stratified based on JAG2$^+$ TANs infiltration in the pooled cohort ($n = 274$), the cutoff value for JAG2$^+$ TANs was determined by the X-tile software. (L) Forest plots for univariate and multivariate Cox regression analysis for the indicated risk factors in patients in pooled cohort ($n = 274$). P value was determined by a log-rank test, and significant P values ($P < 0.05$) were bolded. Abbreviations: CI, confidence interval; CXCR, C-X-C chemokine receptor; DCs, dendritic cells; FIGO, the International Federation of Gynecology and Obstetrics; Foxp3, forkhead box protein P3; GZMB, granzyme B; HGSOC, high-grade serous ovarian cancer; HR, hazard ratio; IFN-γ, interferon-gamma; JAG2, jagged canonical notch ligand 2; LAG3, lymphocyte activation gene-3; LN, lymph node; MFI, mean fluorescence intensity; PBN, peripheral blood neutrophils; PD-1, programmed death 1; PD-L1, programmed cell death ligand 1; TANs, tumor-associated neutrophils; UMAP; uniform manifold approximation and projection.

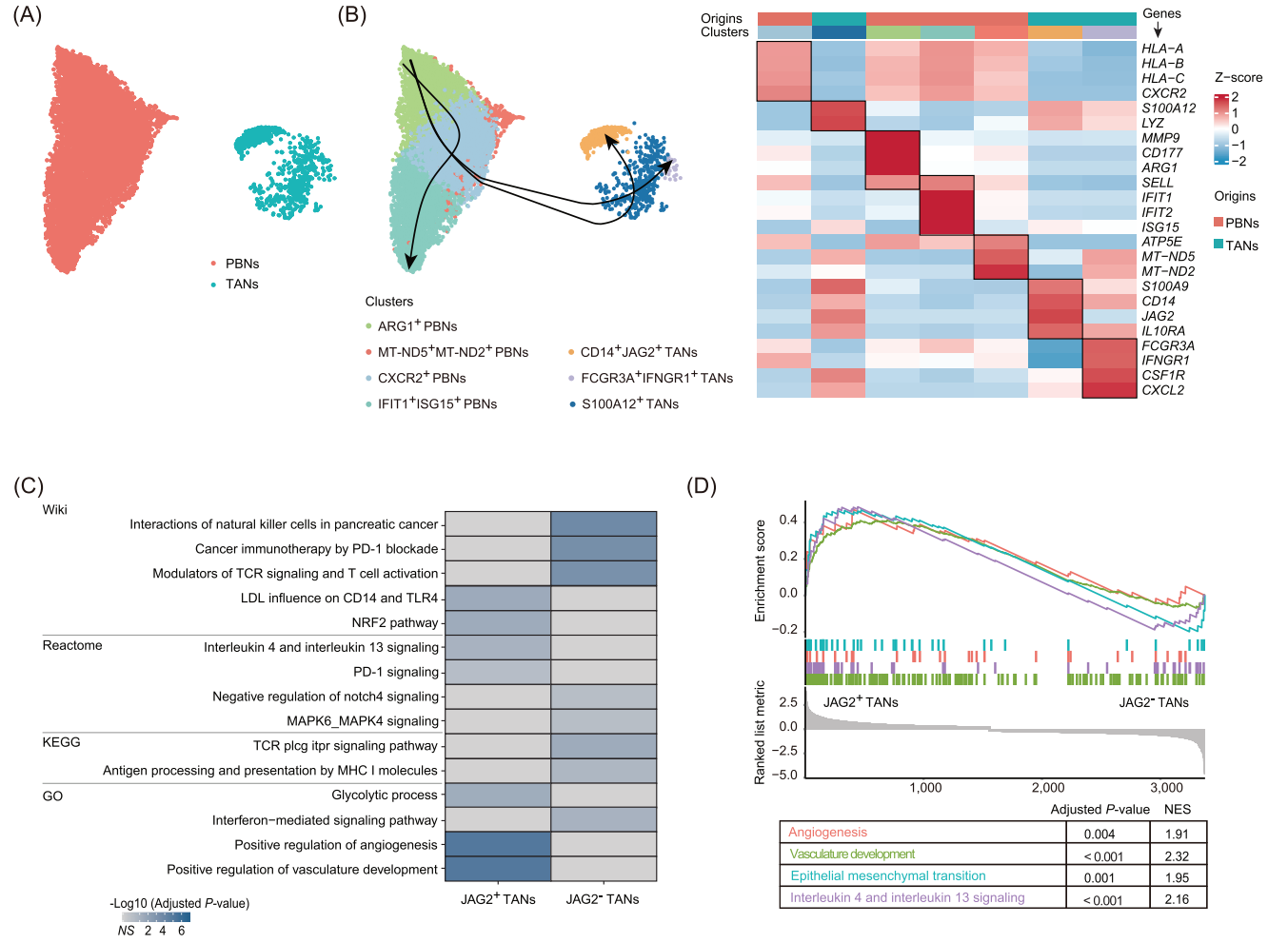

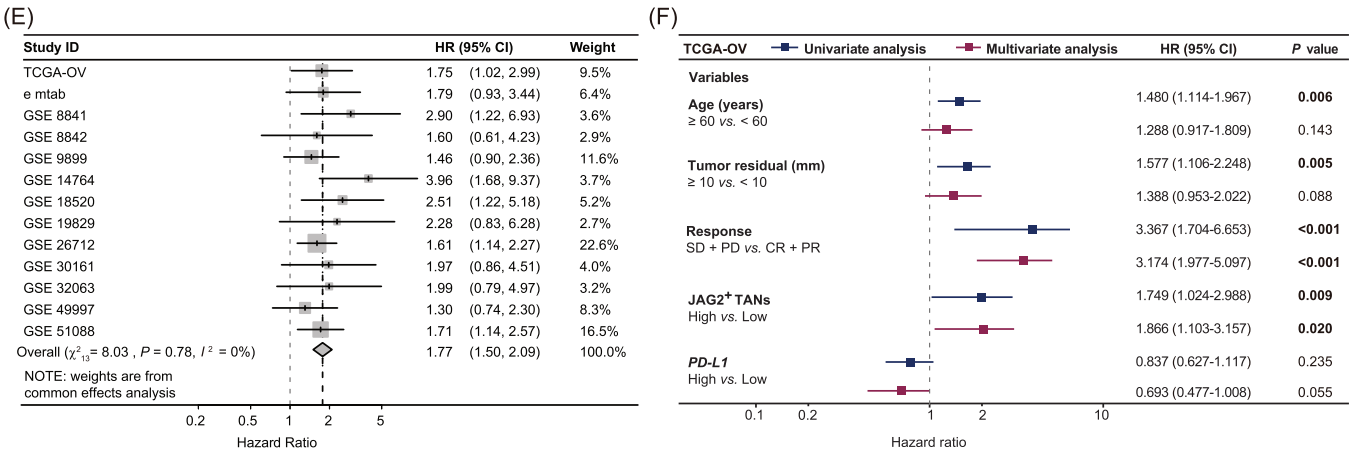

FIGURE 2 Molecular features and prognostic indicator value of JAG2$^+$ TANs. (A) UMAP of combined scRNA-seq data of neutrophils in healthy peripheral blood mononuclear cells and HGSOC tumor tissues. (B) Slingshot on neutrophils (left), revealing three inferred potential trajectories: IFIT1$^+$ISG15$^+$ PBNs, CD14$^+$JAG2$^+$ TANs and FCGR3A$^+$IFNGR1$^+$ TANs. Heatmap (right) of differentially expressed genes (rows) between neutrophils classified into inferred subsets. Bars on the top of the heatmap indicate the site of origin and cell type corresponding to the left UMAP plot. (C) The up- or downregulated genes in the JAG2$^+$ TANs compared to the JAG2$^-$ TANs were enriched for functional pathways as defined by the Wiki, Reactome, KEGG and GO pathway databases. Enrichment score (-log$_{10}$ [adjusted *P* values]) was adjusted by the Benjamini-Hochberg. (D) GSEA result of upregulated angiogenesis, vasculature development, epithelial mesenchymal transition, and interleukin 4 and interleukin 13 signaling in JAG2$^+$ TANs compared with JAG2$^-$ TANs. *P* values were adjusted by the Benjamini-Hochberg method. (E) Forest plot of the pooled HR for OS reflecting the relationship between JAG2$^+$ TANs levels and HGSOC patients. A fixed effects model was used to combine data. The size of the box represents the weight of each study, and the diamond represents the combined effect size

states, such as IFIT1$^+$ISG15$^+$, ARG1$^+$, and S100A12$^+$ neutrophils [6]. We then reconstructed three neutrophil trajectories, starting from ARG1$^+$ PBNs and connecting to MT-ND5$^+$MT-ND2$^+$ PBNs and CXCR2$^+$ PBNs, which branched into IFIT1$^+$ISG15$^+$ PBNs, FCGR3A$^+$IFNGR1$^+$ TANs and CD14$^+$JAG2$^+$ TANs (Figure 2B). We next used the aforementioned scRNA-seq data from tumor tissues to further characterize JAG2$^+$ TANs in HGSOC. GSEA showed that the transcriptional signatures of angiogenesis and immunosuppression pathways were over-represented in JAG2$^+$ TANs within tumor tissues (Figure 2C). Specifically, we found that the gene sets associated with angiogenesis, epithelial mesenchymal transition, and IL-13/IL-4 signaling were enriched in JAG2$^+$ TANs (Figure 2D). Conversely, gene sets related to cancer immunotherapy through PD-1 blockade, T cell receptor signaling, and costimulatory signaling were downregulated (Supplementary Figure S2D).

Moreover, the JAG2$^+$ TAN feature gene set (Supplementary Figure S2E, Supplementary Table S6) was linked to poor prognosis in the TCGA-OV cohort (Supplementary Figure S2F). A meta-survival analysis of 13 independent HGSOC patient cohorts showed that higher JAG2$^+$ TAN infiltration was associated with adverse OS outcomes (HR = 1.77, 95% CI = 1.50-2.09) (Figure 2E). Univariate and multivariate Cox regression analyses further indicated that the JAG2$^+$ TAN feature gene set could serve as an independent prognostic factor for OS in the TCGA-OV cohort (HR = 1.866, 95% CI = 1.103-3.157, $P = 0.020$) (Figure 2F). Taken together, the enrichment of pro-tumor pathways and the association with poor prognosis collectively suggested that JAG2$^+$ TANs exhibited immunosuppressive and pro-tumor phenotypes.

3.3 | JAG2$^+$ TANs correlated with eTreg cell abundance in HGSOC patients

Given the unfavorable impact of JAG2$^+$ TANs, we sought to explore the mechanisms underlying their potential pro-tumor effects. We examined the distinct features of immune contexture related to JAG2$^+$ TANs levels in the training cohort ($n = 120$). There was no correlation between JAG2$^+$ TANs and CD4$^+$ T cells in the JAG2$^+$ TANs^{high} subgroup ($r = 0.041$, $P = 0.767$), while a weak positive correlation was observed between JAG2$^+$ TANs and CD8$^+$ T cells ($r = 0.275$, $P = 0.040$). Specifically, we found that JAG2$^+$ TANs were positively correlated with Tregs merely in the JAG2$^+$ TANs^{high} subgroup ($r = 0.374$, $P = 0.005$) (Figure 3A). Since certain Treg subsets with different functions can impair CD8$^+$ T effector cell (Teff) responses and immune surveillance [41], we analyzed Treg heterogeneity in HGSOC using fresh tumor samples ($n = 21$). It has been demonstrated that ICOS, CTLA4, and CD103 serve as significant markers and targets of immunosuppressive Tregs in tumors [42–44]. Consequently, we utilized them as specific markers to identify distinct subsets of Treg within tumors. We identified three main subpopulations of Tregs with distinct content and profiles: population 1 (ICOS^{mid}CTLA4^{mid}CD103^{mid}), population 2 (ICOS^{low}CTLA4^{low}CD103^{low}), and population 3 (ICOS^{hi}CTLA4^{hi}CD103^{hi}) (Figure 3B-C). Notably, population 3, which exhibited the eTreg phenotype and was positively correlated with JAG2$^+$ TANs (Figure 3D), was abundant in the JAG2$^+$ TANs^{high} subgroup, while population 2 was the predominant subset in the JAG2$^+$ TANs^{low} subgroup (Supplementary Figure S3A). ICOS is highly expressed in the TME, especially on eTregs [39]. We further confirmed the positive correlation between JAG2$^+$ TANs and ICOS$^+$ Tregs (ICOS$^+$Foxp3$^+$) through IHC score in both the training and validation cohorts (Figure 3E, Supplementary Figure S3B-C). Additionally, higher PD-1 expression was observed in the ICOS$^+$ Tregs^{high} subgroup (Supplementary Figure S3D). Interestingly, we also visualized the co-localization of JAG2$^+$ TANs and ICOS$^+$ Tregs through mIHC. We selected 12 regions of interest (ROIs) from six HGSOC tissues to calculate the intercellular distance between ICOS$^+$ Tregs or ICOS$^-$ Tregs and JAG2$^+$ TANs, and found the former was significantly closer to JAG2$^+$ TANs (Figure 3F). To further verify our findings,

and confidence interval. (F) Forest plots for univariate and multivariate Cox regression analysis for the indicated risk factors in patients in the TCGA-OV cohort ($n = 316$). P value was determined by log-rank test, and significant P values ($P < 0.05$) were bolded. Abbreviations: ARG1, arginase 1; CI, confidence interval; CR, complete response; CSF1R, colony stimulating factor 1 receptor; CXCL, C-X-C motif chemokine ligand; CXCR, C-X-C chemokine receptor; FCGR3A, Fc fragment of IgG receptor IIIa; GO, gene ontology; GSEA, gene set enrichment analysis; HGSOC, high-grade serous ovarian cancer; HR, hazard ratio; IFIT1, interferon induced protein with tetratricopeptide repeats 1; IFNGR, interferon-gamma receptor; IL10RA, interleukin 10 receptor subunit alpha; ISG15, interferon-stimulated 15 kDa protein; JAG2, jagged canonical notch ligand 2; KEGG, kyoto encyclopedia of genes and genomes; LDL, low density lipoprotein; LYZ, lysozyme; MAPK, mitogen-activated protein kinase; MHC, major histocompatibility complex; MMP9, matrix metallopeptidase 9; MT-ND, mitochondrially encoded NADH dehydrogenase; NRF2, nuclear factor-erythroid 2 related factor 2; OS, overall survival; PBMC, peripheral blood mononuclear cell; PBN, peripheral blood neutrophil, PD, progressive disease; PD-L1, programmed cell death ligand 1; PR, partial response; SD, stable disease; TAN, tumor-associated neutrophils; TCGA, the cancer genome atlas; TLR4, toll-like receptor 4; UMAP, uniform manifold approximation and projection.

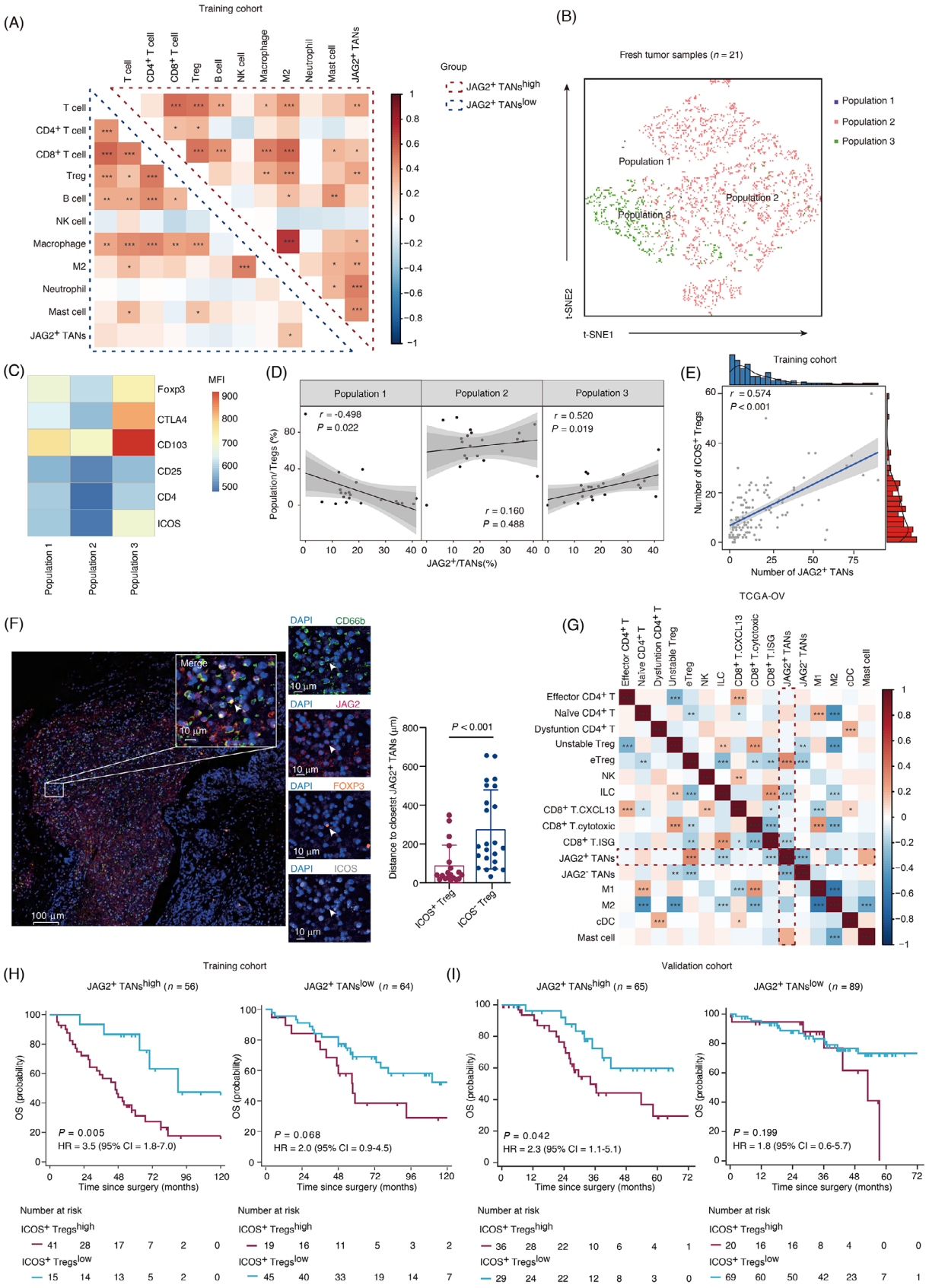

FIGURE 3 JAG2$^+$ TANs correlate with effector Treg cell abundance in patients with HGSOC. (A) Pearson correlation matrix between tumor infiltrating immune cells and JAG2$^+$ TAN subsets derived from HGSOC tissues in training cohort. The legend shows the color change along with the value change in the corresponding Pearson correlation coefficients. Significant correlations are indicated with an asterisk. *, $P < 0.05$, **, $P < 0.01$, ***, $P < 0.001$. (B) *t*-SNE projection and unsupervised FlowSOM clustering of the Treg population in HGSOC tumor

we deconvoluted the immune cell profile in the TCGA-OV cohort, calculated the immune cell proportions, and observed a positive correlation (Pearson's $r = 0.332$, $P < 0.001$) between JAG2$^+$ TANs and eTregs (Figure 3G). Since JAG2$^+$ TANs are associated with an immunosuppressive tumor microenvironment, we wondered if JAG2$^+$ TANs modulate the cytotoxic activity of CD8$^+$ T cells directly. The immunosuppression assays of isolated JAG2$^+$ TANs were performed in vitro. However, purified JAG2$^+$ TANs did not show an enhanced suppressive effect on CD8$^+$ Teffs (Supplementary Figure S3E-F). Survival analysis in the training and validation cohorts demonstrated that high ICOS$^+$ Treg infiltration was associated with poor survival outcomes in the JAG2$^+$ TANs^{high} subgroup, not in the JAG2$^+$ TANs^{low} subgroup (Figure 3H-I). This suggested that Tregs in JAG2$^+$ TAN-enriched tumors might be functionally induced.

3.4 | JAG2$^+$ TANs promoted eTreg cell differentiation in vitro

Tregs can be differentiated from naïve CD4$^+$ T cells in vitro upon T cell receptor activation in the presence of TGF-β and IL-2 [45]. Given the close contact between JAG2$^+$ TANs and eTregs, we hypothesized that JAG2$^+$ TANs could promote the differentiation of eTregs. To prove this hypothesis, we cocultured naïve CD4$^+$ T cells with JAG2$^+$ TANs or JAG2$^-$ TANs extracted from tumor tissues, respectively. We found that CD4$^+$ Treg differentiation was significantly amplified when coculturing with JAG2$^+$ TANs rather than JAG2$^-$ TANs (Supplementary Figure S4A-B). In comparison with the group cocultured with JAG2$^-$ TANs, Tregs cocultured with JAG2$^+$ TANs expressed significantly higher levels of Ki67, IL-10, ICOS, CTLA4, and CD103 (Figure 4A-C), which characterizes eTregs [20, 46, 47]. To confirm the role of JAG2 in inducing the differentiation of eTregs, we treated naïve CD4$^+$ T cells with recombinant JAG2 protein at various doses. Consistently, treatment with recombinant JAG2 led to a significant expansion of CD4$^+$ Tregs (CD4$^+$Foxp3$^+$CD25$^+$). (Figure 4D). Additionally, CD4$^+$ Tregs treated with recombinant JAG2 exhibited higher levels of Ki67, IL-10, ICOS, CTLA4 and CD103 (Figure 4E-F, Supplementary Figure S4C). We hypothesized that JAG2$^+$ TANs promoted eTreg differentiation through modulation of Notch signaling. To test this, we applied LY3039478, a Notch inhibitor that prevents the release of the Notch intracellular domain (NICD) by inhibiting the proteolytic activity of γ-secretase. As a result, LY3039478 effectively reduced eTreg differentiation induced by JAG2$^+$ TANs (Figure 4G-I, Supplementary Figure S4D). Furthermore, reduced proliferation and lower production of cytotoxic cytokines (e.g., IFN-γ) were observed in CD8$^+$ Teffs treated with Tregs pre-cultured with JAG2$^+$ TANs (Figure 4J-K). The proliferation and function of CD8$^+$ Teffs were rescued by adding the Notch inhibitor to the pre-culture system (Figure 4L-M). Altogether, these data indicated that JAG2$^+$ TANs promoted the differentiation of eTregs.

3.5 | JAG2$^+$ TANs promoted eTreg differentiation through Notch-RBPJ signaling in HGSOC

To identify the mechanisms underlying eTreg differentiation driven by JAG2$^+$ TANs, we analyzed the scRNA-seq dataset (GSE180661) and identified five CD4$^+$ T cell clusters, including naïve CD4$^+$ T cells (expressing interleukin-7 receptor [*IL7R*] and transcription factor 7 [*TCF7*]), CD4$^+$

tissues ($n = 21$) identified three distinct subpopulations of Tregs (Populations 1-3). (C) Heatmap depicting MFI of markers for the identified Treg subpopulations. (D) The Spearman correlation between the percentage of JAG2$^+$ TANs out of total TANs and the percentage of each Treg subpopulation out of total Tregs depicted in (C). Each dot represents one patient. (E) Pearson correlation between JAG2$^+$ TANs and ICOS$^+$ Tregs in HGSOC samples of training cohort ($n = 120$). Histograms indicate the numerical values of JAG2$^+$ TANs and ICOS$^+$ Tregs, respectively. (F) The representative spatial relationship map (left) in HGSOC samples was detected by mIHC, showing staining for CD66b (green), JAG2 (red), ICOS (grey), FOXP3 (orange), and DAPI (blue). The distance from ICOS$^+$ and ICOS$^-$ Tregs to the closest JAG2$^+$ TANs (right) was compared (unpaired *t*-test). Scale bar, 100 μm and 10 μm. (G) Pearson correlation matrix of immune cell types inferred by CIBERSORTx in the TCGA-OV cohort. *, $P < 0.05$, **, $P < 0.01$, ***, $P < 0.001$. (H-I) Kaplan-Meier curves for overall survival of patients stratified by ICOS$^+$Foxp3$^+$ cell levels in training cohort (H) and validation cohort (I) with high or low JAG2$^+$ TANs. The cutoff values of both ICOS$^+$Foxp3$^+$ cells and JAG2$^+$ TANs were determined by the X-tile software. Statistical *P* value was calculated using the log-rank test. Abbreviations: cDC, conventional dendritic cells; CI, confidence interval; CIBERSORTx, cell-type identification by estimating relative subsets of RNA transcripts x; CTLA4, cytotoxic T-lymphocyte associated antigen 4; CXCL, C-X-C motif chemokine ligand; eTreg, effector regulatory T cell; FlowSOM, self-organizing maps of flow cytometry data; FOXP3, forkhead box protein P3; HR, hazard Ratio; ICOS, inducible T-cell co-stimulator; ILC, innate lymphoid cell; ISG, interferon-stimulated gene; JAG2, jagged canonical notch ligand 2; M1, M1-like tumor-associated macrophages; M2, M2-like tumor-associated macrophages; MFI, mean fluorescent intensity; mIHC, multiplex immunehisto-chemical; NK, natural killer cell; TAN, tumor-associated neutrophils; TCGA, the cancer genome atlas; Treg, regulatory T cell; t-SNE, t-distributed stochastic neighbor embedding.

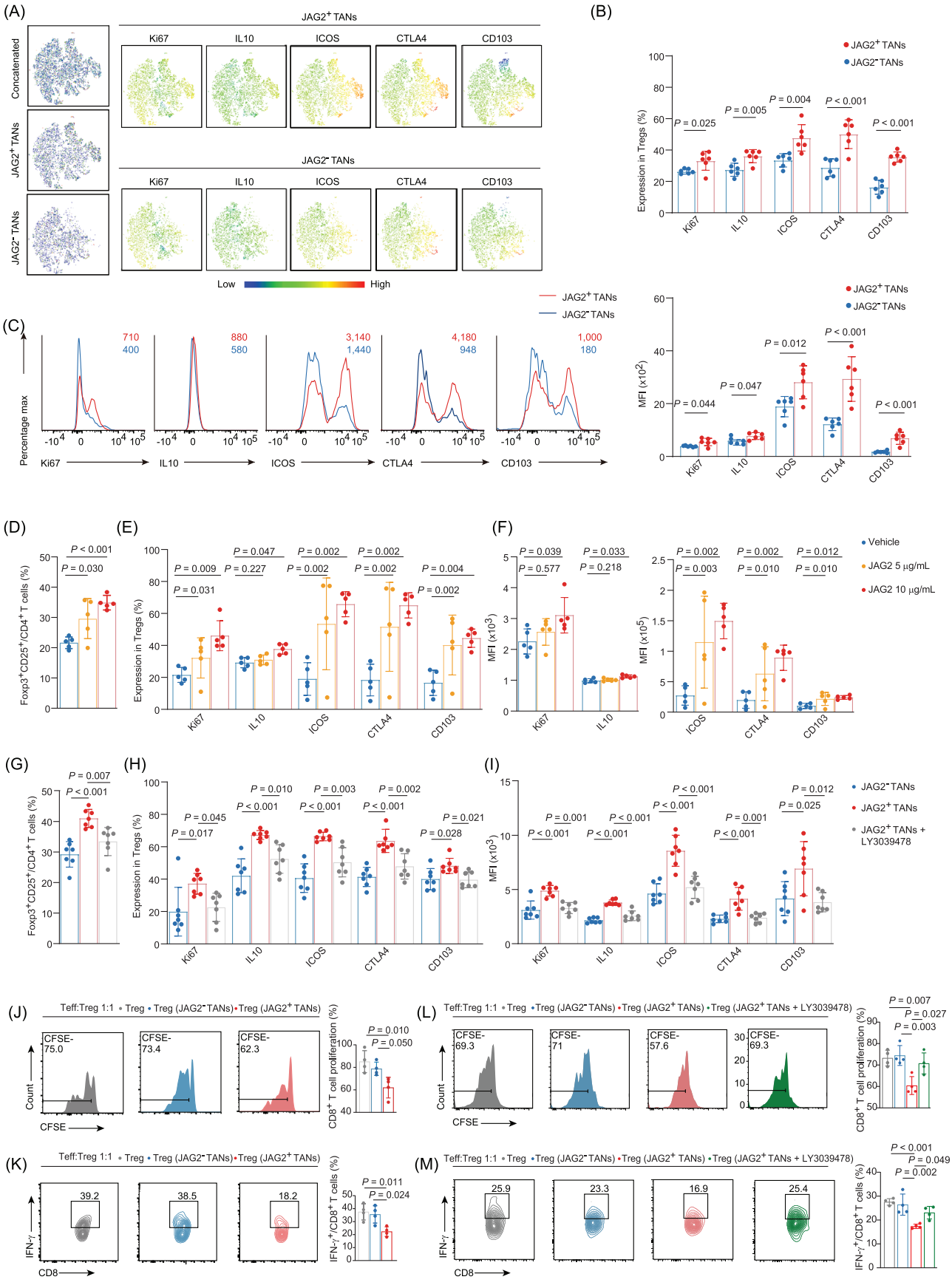

Teff cells (expressing *CCL5* and killer cell lectin like receptor B1 [*KLRB1*]), dysfunction CD4$^+$ T cells (expressing dysfunctional T cell markers C-X-C motif chemokine ligand 13 [*CXCL13*], TOX high mobility group box family member 2 [*TOX2*], and hepatitis A virus cellular receptor 2 [*HAVCR2*], unstable Treg cells (expressing *FOXP3, IL2RA*, and *IL6R*) [48, 49] and eTregs (expressing *FOXP3, IL2RA, IL10, ICOS, CTLA4*, integrin alpha E [*ITGAE/CD103*], and marker of proliferation Ki-67 [*MKI67*]) (Figure 5A-B). Transcriptional gene expressions obtained from the identified CD4$^+$ T cell subpopulations were compared to a reported pan-cancer Treg gene signature (Magnuson signature), which has been previously demonstrated to represent tumor-infiltrating Tregs exhibiting potent immunosuppressive functionality [32]. We demonstrated significantly elevated activity of the Magnuson signature in eTregs compared to other CD4$^+$ T cell clusters. (Figure 5C). Analysis of DEGs and GO revealed that, in addition to the negative regulation of T cell proliferation, activation, and cytotoxicity, eTregs also have the potential to upregulate IL-10 production (Supplementary Figure S5A-B). Accordingly, the eTreg feature gene set was identified (Supplementary Table S7). Stratifying patients with high or low eTreg feature gene expression scores of JAG2$^+$ TANs in the TCGA-OV cohort, we found that higher eTreg infiltration was associated with significantly poor survival outcomes only in the JAG2$^+$ TAN^{high} subgroup (Supplementary Figure S5C-D). Trajectory inference analysis further confirmed that tumor-infiltrating eTregs represented the terminal differentiated state (Figure 5D).

To further investigate the potential interplay, we conducted cell-cell interaction analysis using NicheNet [50]. Notably, JAG2$^+$ TANs showed significant interactions with eTregs through JAG2-Notch1/Notch2 signaling (Figure 5E). Following ligand binding to the Notch receptor, the extracellular cleavage of Notch is triggered, a process catalyzed by ADAM family metalloproteases (e.g., ADAM10 and ADAM17) [51]. To investigate the regulatory effects of JAG2$^+$ TANs on the transcriptional programs of eTregs, we employed JAG2$^+$ TANs as signal-sending cells and eTregs as target cells. We observed that ADAM17, identified as one of the predicted active ligands associated with JAG2$^+$ TANs, is involved in their interaction with genes in eTregs. eTreg-related genes, such as interleukin 2 receptor subunit alpha (*IL2RA*), have the potential to be regulated by JAG2$^+$ TANs (Figure 5F). Additionally, we noticed that RBPJ was also a target of JAG2$^+$ TANs on eTregs (Figure 5F). RBPJ is a major transcriptional effector of Notch signaling and forms an activator complex with NICD [18], highlighting the critical role of the Notch-RBPJ axis in eTreg differentiation mediated by JAG2$^+$ TANs. To validate the importance of Notch signaling in eTreg differentiation, we performed siRNA-mediated knockdown of *RBPJ* in naïve CD4$^+$ T cells (Supplementary Figure S5E). This knockdown resulted in a reduced differentiation of eTregs mediated by JAG2$^+$ TANs (Supplementary Figure S5F). To further confirm that JAG2 acts through Notch signaling, we first analyzed the expression of Notch receptors on various cell types using FCM. The results demonstrated that Tregs exhibit significantly higher expression

FIGURE 4 JAG2$^+$ TANs promote eTreg differentiation in vitro. (A-B) *t*-SNE plots (A) and quantification of the percentage of expression (B) of Ki67, IL10, ICOS, CTLA4 and CD103 on Treg cells following cocultured with JAG2$^-$ TANs or JAG2$^+$ TANs extracted from tumor tissues. (C) Representative histograms (left) and quantification (right) of the MFI of Ki67, IL10, ICOS, CTLA4 and CD103 expression on Treg cells in (A). (D) Quantification of the percentage of Foxp3$^+$CD25$^+$ cells in CD4$^+$ T cells following the treatment with increased concentrations of recombinant human JAG2 (5, 10 μg/mL). (E) Quantification of the percentage of Ki67, IL10, ICOS, CTLA4 and CD103 expression in Treg cells following the treatment with increased concentrations of recombinant human JAG2 (5, 10 μg/mL). (F) Quantification of the MFI of Ki67, IL10, ICOS, CTLA4 and CD103 expression in Treg cells following the treatment with increased concentrations of recombinant human JAG2 (5, 10 μg/mL). (G) Quantification of the percentage of Foxp3$^+$CD25$^+$ cells in CD4$^+$ T cells following cocultured with JAG2$^-$ TANs or JAG2$^+$ TANs in the absence or presence of Notch inhibitor (LY3039478). (H) Quantification of the percentage of Ki67, IL10, ICOS, CTLA4 and CD103 expression in Treg cells following cocultured with JAG2$^-$ TANs or JAG2$^+$ TANs in the absence or presence of Notch inhibitor (LY3039478). (I) Quantification of the MFI of Ki67, IL10, ICOS, CTLA4 and CD103 expression in Treg cells following cocultured with JAG2$^-$ TANs or JAG2$^+$ TANs in the absence or presence of Notch inhibitor (LY3039478). (J) Representative histograms and cumulative data showing CD8$^+$ T cell proliferation assessed by CFSE dilution after cocultured with Treg cells, either precultured with JAG2$^-$ TANs or JAG2$^+$ TANs. (K) Representative flow cytometry plots and quantification of the percentage of IFN-γ^+ CD8$^+$ T cells among total CD8$^+$ T cells corresponding in (J). (L) Representative histograms and cumulative data showing CD8$^+$ T cell proliferation assessed by CFSE dilution after cocultured with Treg cells. The Treg cells were either pre-cultured with JAG2$^-$ TANs or JAG2$^+$ TANs, and either with or without the addition of a LY3039478 in the preculture system. (M) Representative flow cytometry plots and quantification of the percentage of IFN-γ^+ CD8$^+$ T cells among total CD8$^+$ T cells corresponding in (L). Statistical analyses were performed by two-tailed unpaired Student's *t*-test (B, C) and one-way ANOVA with Tukey's post hoc test (D-M). Bar graphs show mean ± standard deviation. Data are from the integration of two independent experiments (B-C) or the results of one representative experiment out of three independent experiments (D-M). Abbreviations: CFSE, carboxyfluorescein succinimidyl ester; CTLA4, cytotoxic T-lymphocyte associated antigen 4; Foxp3, forkhead box protein P3; ICOS, inducible T-cell co-stimulator; IFN-γ, interferon-gamma; IL10, interleukin-10; JAG2, jagged canonical notch ligand 2; MFI, mean fluorescent intensity; TAN, tumor-associated neutrophil; Teff, effector T cell; Treg, regulatory T cell, t-SNE, t-distributed stochastic neighbor embedding.

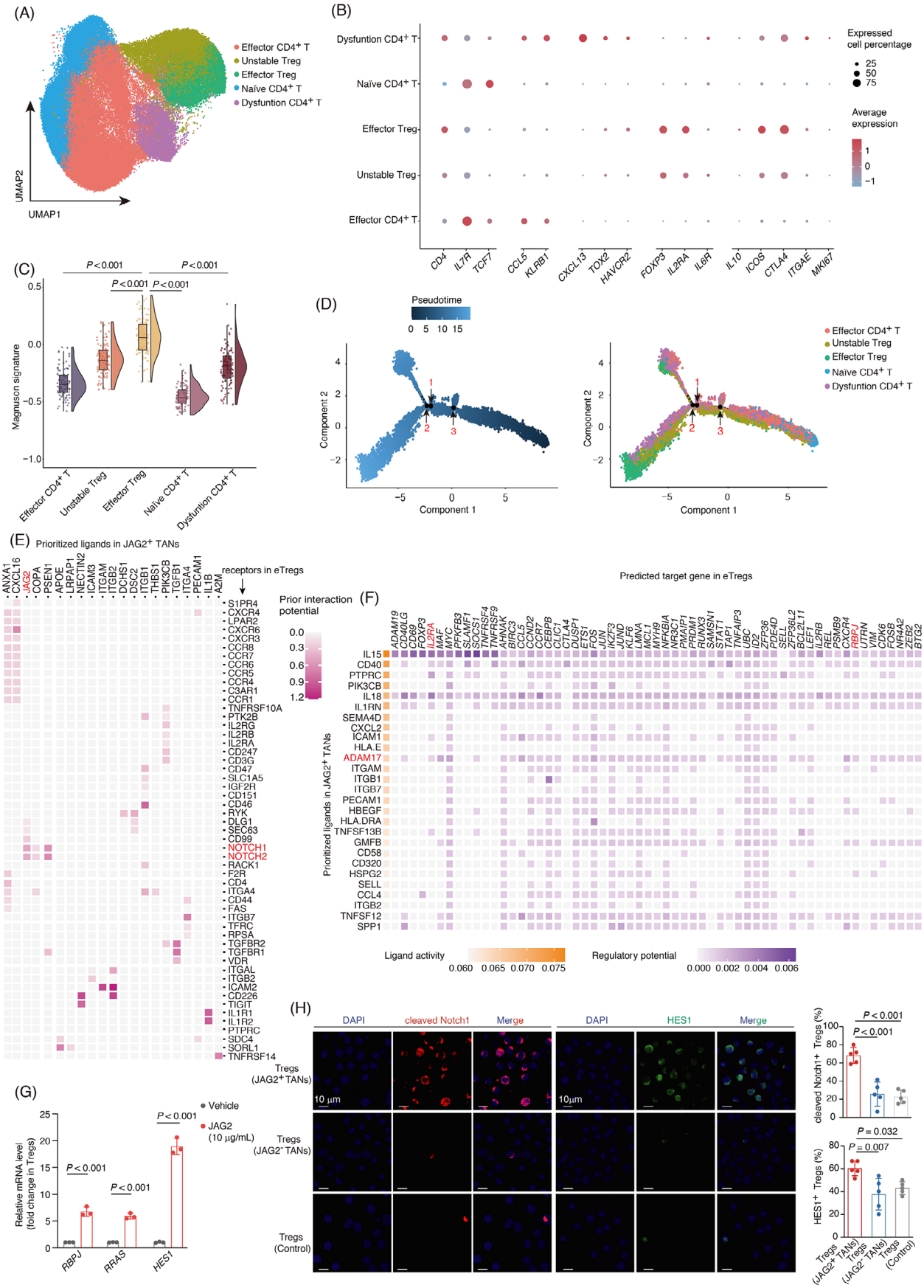

of Notch1 compared to other cell populations (Supplementary Figure S5G). Considering that the expression of Notch-driven transcripts *RBPJ*, RAS related (*RRAS*), and *HES1* has been utilized to demonstrate activation of the Notch pathway [52], we next purified Tregs from naive $CD4^+$ T cells treated with or without JAG2 protein and quantified the levels of the aforementioned Notch-driven transcripts in Tregs using RT-qPCR. Tregs treated with recombinant JAG2 protein exhibited higher *RBPJ* expression, along with upregulation of *RRAS* and *HES1* (Figure 5G). Additionally, we assessed endogenous levels of the Notch1 intracellular domain (NICD1) and HES1 by immunofluorescence. Consistent with our findings, higher levels of cleaved Notch1 and HES1 were observed in Tregs co-cultured with $JAG2^+$ TANs (Figure 5H). Given that Notch controls numerous differentiation processes, we explored the TFs involved in eTreg differentiation mediated by Notch signaling. Using SCENIC analysis of scRNA-seq data, we identified the top eleven TFs with the highest regulon activity scores for the eTreg cluster; PR/SET domain 1 or B lymphocyte-induced maturation protein 1 (PRDM1/BLIMP1, PRDM1_extended) emerged as core TFs regulating the eTregs signature (Supplementary Figure S5H). Consistent with our findings, previous studies have also shown that Blimp-1 is essential for the generation of eTreg cells [23, 24].

3.6 | $JAG2^+$ TANs might be a predictor of resistance to ICIs and a potential target to enhance the response to anti-PD-1 therapy

As previously demonstrated, the gene set associated with response to cancer immunotherapy by PD-1 blockade was significantly upregulated in $JAG2^-$ TANs (Figure 2C). In the next stage, we tried to elucidate the impact of $JAG2^+$ TANs on ICI therapy. To assess the early immunological response of HGSOC to PD-1 blockade, we employed short-term organoid culture and ex vivo intervention experiments. This analysis revealed two broad groups of HGSOC tumors: a larger group (22 out of 30 tumors, referred to as non-responders) exhibited minor treatment-induced changes in cytotoxic activity after ex vivo PD-1 blockade, while a smaller group of tumors (8 out of 30, referred to as responders) showed a significant increase in cytotoxic activity (Figure 6A). Notably, more $JAG2^+$ TANs accumulated in non-responder tumors following anti-PD-1 treatment (Figure 6B). Furthermore, in the $JAG2^+$ $TANs^{low}$ subgroup, ex vivo PD-1 blockade induced significant changes in the apoptosis of tumor cells and cytotoxic activity of $CD8^+$ T cells, whereas this effect was not observed in the $JAG2^+$ $TANs^{high}$ subgroup (Figure 6C-D). We next examined the effect of dual blockade of PD-1 and Notch on the cytotoxic activity of $CD8^+$ T cells compared to the PD-1 blockade alone. We observed prominent increases in the cytotoxic activity of $CD8^+$ T cells in the $JAG2^+$ $TANs^{high}$ subgroup, while no significant changes were noted in the $JAG2^+$ $TANs^{low}$ subgroup (Figure 6E). Additionally, we detected a decrease in IL-10, ICOS, CTLA4, and CD103 expression on Tregs in the $JAG2^+$ $TANs^{high}$ subgroup following dual blockade of PD-1 and Notch signaling (Figure 6F).

We next examined the role of $JAG2^+$ TANs in clinical immunotherapy data. In five cohorts receiving immunotherapy spanning skin cutaneous melanoma, urothelial carcinoma, renal cell carcinoma, and non-small cell lung cancer patients, higher $JAG2^+$ TAN infiltration consistently indicated unfavorable survival outcomes with

FIGURE 5 $JAG2^+$ TANs promote eTreg differentiation in HGSOC tissues. (A) UMAP plot of 70,352 $CD4^+$ T cells from scRNA-seq data in HGSOC showing five colored clusters. (B) Relative expression bubble plot of selected genes known to be associated with $CD4^+$ T cell subsets. The color of each dot represents the average normalized expression from high to low. The size of each dot represents the expressed cell percentage. (C) Raincloud plot showing the comparison of Magnuson signature in each $CD4^+$ T cell subsets identified in (A). (D) Pseudotime trajectory for $CD4^+$ T cells from (A) in two-dimensional state-space defined by monocle 2. The degree of color represented pseudotime (left), and colors represented different identified $CD4^+$ T cell subsets (right). The red text indicated differentiation nodes of cell states in the trajectory. (E) Heatmap showing the interactions between the prioritized ligand in $JAG2^+$ TANs and the receptors expressed in the eTreg. (F) Heatmap of the activity (left), and regulatory potential (right) of the prioritized ligands in $JAG2^+$ TANs promoting the eTreg program. (G) The expression levels of *RBPJ*, *RRAS* and *HES1* mRNA in Treg cells treated with either recombinant human JAG2 (10 μg/mL) or vehicle, as detected by qRT-PCR analyses. (H) Immunofluorescence images (left) and quantification (right) showing endogenous levels of cleaved Notch1 and HES1 in Tregs induced by $JAG2^+$/$JAG2^-$ TANs or vehicle. Scale bar, 10 μm. Data were analyzed by two-tailed unpaired Student's *t*-test (G) one-way ANOVA with Tukey's post hoc test (H). Bar graphs show mean ± standard deviation. Abbreviations: CCL5, C-C Motif Chemokine Ligand 5; CTLA4, cytotoxic T-lymphocyte associated antigen 4; CXCL, C-X-C motif chemokine ligand; FOXP3, forkhead box protein P3; HAVCR2, hepatitis a virus cellular receptor 2; HES1, hairy and enhancer of split-1; ICOS, inducible T-cell co-stimulator; IL10, interleukin-10; IL2RA, interleukin 2 receptor subunit alpha; IL6R, interleukin 6 receptor; IL7R, interleukin 7 receptor; ITGAE, integrin alpha E; JAG2, jagged canonical notch ligand 2; KLRB1, killer cell lectin like receptor B1; qRT-PCR, quantitative real-time polymerase chain reaction; RBPJ, recombination signal binding protein for immunoglobulin kappa J region; RRAS, RAS related gene; TAN, tumor-associated neutrophil; TCF7, transcription factor 7; TOX2, TOX high mobility group box family member 2; Treg, regulatory T cell; UMAP, uniform manifold approximation and projection.

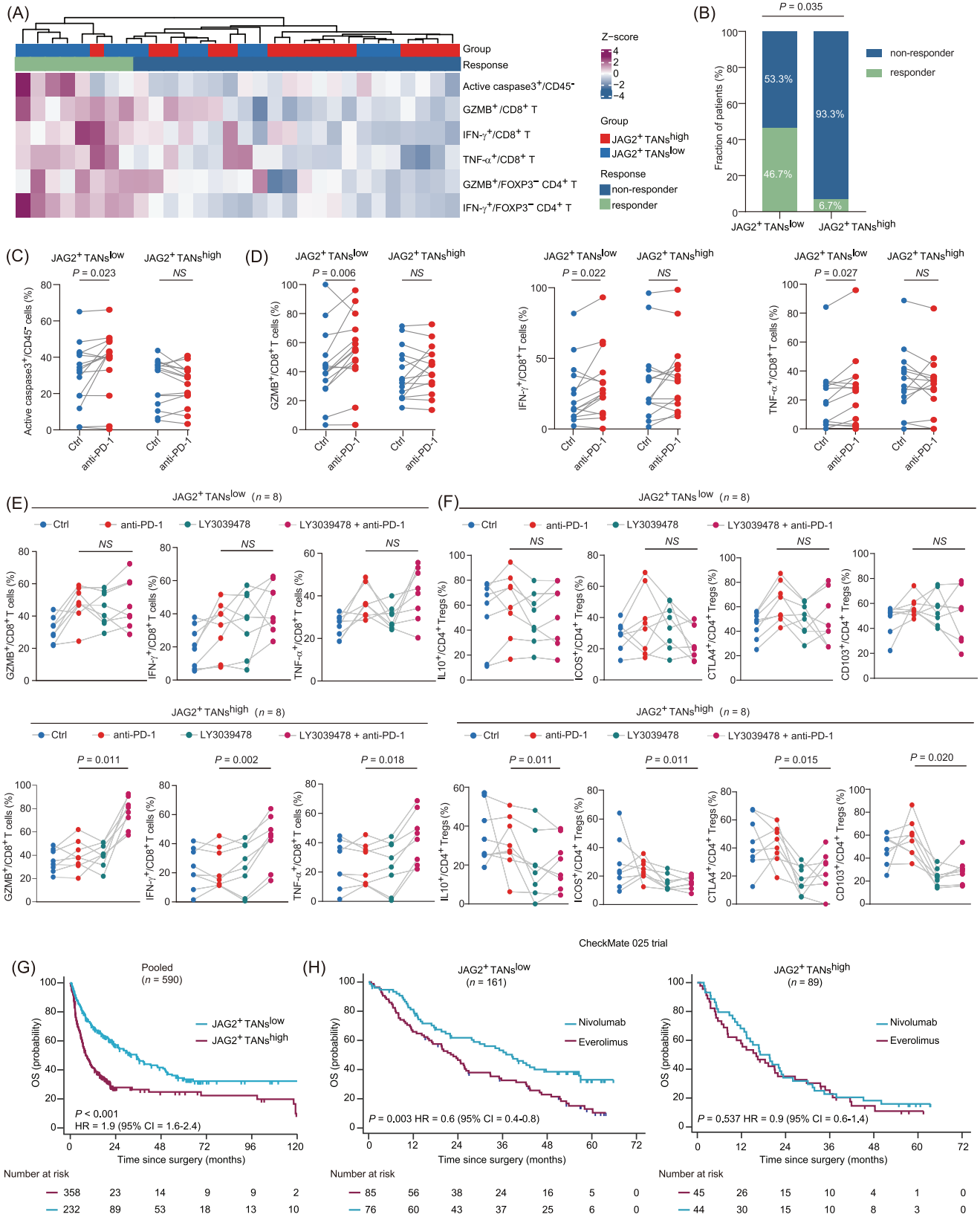

FIGURE 6 JAG2$^+$ TANs could serve as a predictive marker for resistance to ICIs and as a potential target to improve the response to anti-PD-1 therapy. (A) Hierarchical clustering of response to anti-PD-1 treatment according to the percentage of cytotoxic cytokines expression in CD8$^+$ T cells and Foxp3$^-$CD4$^+$ T cells and cleaved caspase-3$^+$ in CD45$^-$ cells ($n = 30$). Samples were clustered using complete linkage and Euclidean distance. (B) The proportion of anti-PD-1 therapy responder in each JAG2$^+$ TAN subgroup. (C-D) Quantification of the percentage of cleaved caspase-3$^+$ cells in CD45$^-$ cells (C) and cytotoxic cytokines (GZMB$^+$, IFN-γ^+, TNF-α^+) in CD8$^+$ T cells (D) in the isotype- and anti-PD-1 antibody-treated tumors, stratified by binary JAG2$^+$ TANs based on median value ($n = 15$). (E) Quantification of the percentage of

ICI therapy across tumor types and treatment regimens (Supplementary Figure S6A). We integrated these cohorts into a pooled set. Survival analysis confirmed that patients with higher JAG2$^+$ TAN infiltration experienced worse survival outcomes in the pooled set (Figure 6G, Supplementary Figure S6B). Given the relation between JAG2$^+$ TANs and unfavorable survival outcomes, we hypothesized that tumors with low levels of JAG2$^+$ TANs might be more sensitive to ICI therapy. Supporting this, in the JAG2$^+$ TANs^{low} subgroup from the CheckMate 025 clinical trial (renal cell carcinoma), ICI therapy resulted in prolonged OS compared to non-ICI therapy (Figure 6H). Collectively, these data confirmed that JAG2$^+$ TAN infiltration could be a potential predictor in patients receiving ICI therapies.

3.7 | Target inhibition of Notch signaling sensitized anti-PD-1 immunotherapy in vivo

We have established that Notch signaling regulates the differentiation of eTregs. A critical unanswered question is whether therapeutic blockade of Notch signaling can potentiate immunotherapy efficacy in vivo. We further explored the effect of the Notch inhibitor LY3039478 on the therapeutic response to anti-PD-1 blockade in vivo. Notably, the combination of LY3039478 and anti-PD-1 blockade significantly retarded tumor progression in a subcutaneous model (Figure 7A, Supplementary Figure S7A-B). This combination therapy resulted in a marked increase in the proportion of progenitor-exhausted CD8$^+$ T (Tpex) cells (PD-1$^+$TCF1$^+$) (Figure 7B), which are essential for responding to PD-1 blockade therapy [53]. PD-1 blockade triggers a transient proliferative expansion of Tpex cells, which ultimately terminally differentiate into Tex cells exhibiting augmented effector functionality in inflammatory cytokine production [54]. Consistently, the combination of LY3039478 and anti-PD-1 promoted the proliferation and cytotoxic activity of CD8$^+$ tumor-infiltrating lymphocytes (Figure 7C, Supplementary Figure S7C). In contrast, this combination treatment resulted in a decrease in the percentage of Tregs (Figure 7D) and reduced the expression of their markers, including Ki67, IL-10, CTLA4, ICOS, and CD103 (Figure 7E). Moreover, dual blockade of PD-1 and Notch did not decrease JAG2$^+$ TANs in HM1 tumors, although the proportion of JAG2$^+$ TANs varied among the mice (20.5% ± 10.5%) (Supplementary Figure S7D). Together, these data demonstrate that the Notch inhibitor, by inhibiting eTreg differentiation, enhances the response to anti-PD-1 immunotherapy in vivo.

To mimic the dissemination of HGSOC into the peritoneum, we employed an intraperitoneal xenograft model (Supplementary Figure S7E). We utilized luciferase-expressing tumor cells to measure spontaneous peritoneal metastasis, with bioluminescent signals quantifying the metastatic tumor burden. Combination therapy significantly reduced the formation of hemorrhagic ascites and secondary tumor deposits (Figure 7F-G, Supplementary Figure S7F-G), and caused prolonged survival (Figure 7H). Similarly, combination therapy increased the percentage of Tpex and intermediate-exhausted T (Tex-int) cells in tumors, while not affecting Tex cells (Supplementary Figure S7H). Additionally, the proliferation of Tpex was significantly enhanced (Supplementary Figure S7I). This combination therapy appeared to maintain Tpex cells and promote their differentiation. We also observed alterations in the proliferation and cytotoxic activities of CD8$^+$ T cells (Figure 7I-J, Supplementary Figure S7J) and the percentage of eTregs (Figure 7K-M), consistent with findings in the subcutaneous tumor model. Notably, we observed a reduction in JAG2$^+$ TANs after combination therapy in ID8agg-Luc tumors, with the proportion of JAG2$^+$ TANs varying among individual mice (27.2% ± 10.5%) (Supplementary Figure S7K). Finally, we investigated the therapeutic potential of a JAG2-blocking antibody. Treatment of tumor-bearing mice with anti-JAG2 combined with

cytotoxic cytokines (GZMB$^+$, IFN-γ^+, TNF-α^+) in CD8$^+$ T cells in the isotype, anti-PD-1 antibody, LY3039478 and LY3039478 + anti-PD-1 antibody-treated tumors with binary JAG2$^+$ TANs stratified by median value ($n = 8$). (F) Quantification of the percentage of IL10$^+$, ICOS$^+$, CTLA4$^+$ and CD103$^+$ cells among CD4$^+$ Treg cells in tumors in the isotype, anti-PD-1 antibody, LY3039478 and LY3039478 + anti-PD-1 antibody-treated tumors with binary JAG2$^+$ TANs stratified by median value ($n = 8$). (G) Kaplan-Meier curve for overall survival of patients receiving ICI therapy for pooled data, the cutoff value for JAG2$^+$ TANs was chosen with the lowest P value. (H) Kaplan-Meier curves for overall survival (OS) by treatment in patients with RCC from CheckMate 025 clinical trial, stratified by low and high levels of JAG2$^+$ TANs levels (cutoff value determined by the X-tile software). Overall survival was significantly improved with ICI therapy in patients with low JAG2$^+$ TANs ($P = 0.003$) but not in those with high JAG2$^+$ TANs ($P = 0.537$). Data were analyzed by $\chi 2$ test (B), paired Student's t-test (C and D), one-way ANOVA with Tukey's post hoc test (E and F), log-rank test (G and H). Abbreviations: CI, confidence interval; CTLA4, cytotoxic T-lymphocyte associated antigen 4; Ctrl, control; GZMB, granzyme B; HR, hazard ratio; ICI, immune checkpoint inhibitor; ICOS, inducible T-cell co-stimulator; IFN-γ, interferon-gamma; IL10, interleukin-10; JAG2, jagged canonical notch ligand 2; OS, overall survival; PD-1, programmed death 1; RCC, renal cell carcinoma; TAN, tumor-associated neutrophils; TNF-α, tumor necrosis factor-α.

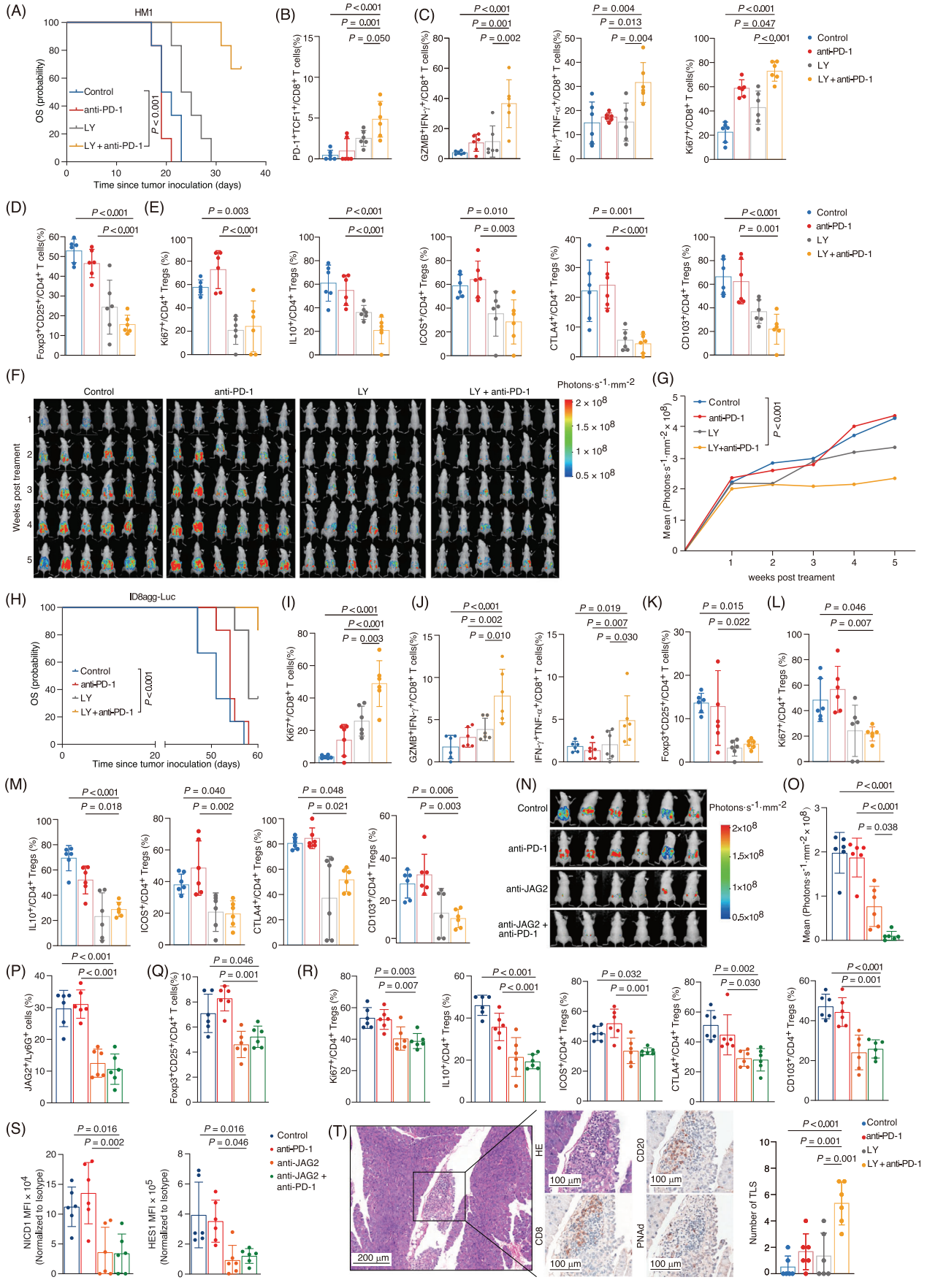

anti-PD-1 induced significant anti-tumor effects in ID8agg-Luc tumors (Figure 7N-O). As expected, anti-JAG2 plus anti-PD-1 treatment decreased the proportion of intratumoral JAG2$^+$ TANs (Figure 7P). In line with the protective role of Notch inhibitor, higher proportions of cytotoxic CD8$^+$ T cells and Tpex (Supplementary Figure S7L-O) and a lower proportion of eTregs (Figure 7Q-R) were observed in tumor-bearing mice treated with the combination of anti-JAG2 and anti-PD-1. Furthermore, we assessed whether anti-JAG2 treatment elicits anti-tumor effects through similar mechanisms as the Notch inhibitor. Tregs from tumor-bearing mice treated with anti-JAG2 exhibited reduced NICD1 and HES1 expression compared to controls and those receiving anti-PD-1 treatment (Figure 7S, Supplementary Figure S7P). Our findings suggest that JAG2 blockade facilitates the reprogramming of intratumoral Tregs, highlighting an intrinsic role for Notch signaling in the differentiation of eTregs.

Studies have demonstrated that the presence of an activated immune niche surrounding Tpex cells is present in both murine and human samples [55, 56]. The formation of tertiary lymphoid structures (TLSs) was enhanced in the combination therapy group (LY3039478 plus anti-PD-1) (Figure 7T), correlating with the increase in Tpex cells (Supplementary Figure S7Q). Consequently, combination therapy might reshape the immune contexture, including TLSs, thereby contributing to an effective response to anti-PD-1 blockade.

4 | DISCUSSION

Although the heterogeneity of neutrophils is increasingly recognized, many important questions remain regarding their roles in cancer. Targeting all neutrophil subsets may not constitute a successful therapeutic approach, raising critical questions about which subsets drive pro-tumor effects. Our findings uncover the mechanistic contribution of JAG2$^+$ TANs to immune evasion in the tumor microenvironment. Specifically, JAG2$^+$ TANs regulated eTreg cells, facilitating their differentiation from naïve CD4$^+$ T cells through the activation of Notch signaling. Previous studies have described the redundant functions of Notch1 and Notch2 [57], but whether this functional interchange applies to Tregs remains unclear. The increased expression of Notch1 relative to Notch2, along with differential ligand affinities, may explain the more pronounced role of Notch1 in the differentiation of eTregs. Targeting JAG2 and employing Notch inhibitors activated anti-tumor immunity by inducing functional reprogramming of eTreg

FIGURE 7 Target inhibition of Notch signaling sensitizes anti-PD-1 immunotherapy in vivo. (A) Kaplan-Meier survival curves in mice with subcutaneous tumor of HM1 cells, treated with control IgG, anti-PD-1 antibody, LY3039478, and LY3039478 plus anti-PD-1 antibody. (B) Quantification of the percentage of Tpex (PD-1$^+$TCF1$^+$) cells in CD8$^+$ T cells within tumors of HM1 cells. (C) Quantification of the percentage of CD8$^+$ T cells expressing cytotoxic cytokines and Ki67 within tumors of HM1 cells. (D) Quantification of the percentage of Foxp3$^+$CD25$^+$ cells in CD4$^+$ T cells within tumors of HM1 cells. (E) Quantification of the percentage of Ki67$^+$, IL-10$^+$, CTLA4$^+$, ICOS$^+$ and CD103$^+$ cells in CD4$^+$ Tregs within tumors of HM1 cells. (F) Representative bioluminescence images of mice with intraperitoneal implantation of 1×10^7 ID8agg-Luc cells, 1, 2, 3, 4, and 5 weeks after treatment with control IgG, anti-PD-1 antibody, LY3039478, and LY3039478 plus anti-PD-1 antibody. (G) Luciferase signal intensities at weeks 1, 2, 3, 4 and 5 within tumors of ID8agg-Luc cells treated as in (F). (H) Kaplan-Meier survival curves in mice with intraperitoneal implantation of ID8agg-Luc cells. (I) Quantification of the percentage of Ki67$^+$ cells in CD8$^+$ T cells within tumors of ID8agg-Luc cells treated as in (F). (J) Quantification of the percentage of cytotoxic cytokines in CD8$^+$ T cells within tumors of ID8agg-Luc cells treated as in (F). (K) Quantification of the percentage of Foxp3$^+$CD25$^+$ cells in CD4$^+$ T cells within tumors of ID8agg-Luc cells treated as in (F). (L) Quantification of the percentage of Ki67$^+$ cells in CD4$^+$ Treg cells within tumors of ID8agg-Luc cells treated as in (F). (M) Quantification of the percentage of IL10$^+$, CTLA4$^+$, ICOS$^+$, and CD103$^+$ cells in CD4$^+$ Treg cells within tumors of ID8agg-Luc cells treated as in (F). (N) Representative bioluminescence images of mice with intraperitoneal implantation of 1×10^7 ID8agg-luc cells, treated with control IgG, anti-PD-1 antibody, anti-JAG2 antibody, and anti-PD-1 antibody plus anti-JAG2 antibody. (O) Luciferase signal intensities at week 2 within tumors of ID8agg-Luc cells treated as in (N). (P) Quantification of the percentage of JAG2$^+$ TANs within tumors of ID8agg-Luc cells treated as in (N). (Q) Quantification of the percentage of Foxp3$^+$CD25$^+$ cells in CD4$^+$ T cells within tumors of ID8agg-Luc cells treated as in (N). (R) Quantification of the percentage of Ki67$^+$, IL10$^+$, CTLA4$^+$, ICOS$^+$ and CD103$^+$ cells in Treg cells within tumors of ID8agg-Luc cells treated as in (N). (S) Quantification of the MFI of NICD1 and HES1 in Treg cells within tumors of ID8agg-Luc cells treated as in (N). (T) Representative HE and immunohistochemistry images of CD20, CD8 and PNAd in tumors with the treatment of LY3039478 plus anti-PD-1 antibody (left), quantification of the number of TLS in tumors of ID8agg-Luc cells after treatment with control IgG, anti-PD-1 antibody, LY3039478, and LY3039478 plus anti-PD-1 antibody (right). Data were analyzed by log-rank test (A and H), one-way ANOVA with Tukey's post hoc test (B-E, I-M, O-T), and two-way ANOVA with Sidak's multiple comparison tests (G). Bar graphs show mean ± standard deviation. Abbreviations: CTLA4, cytotoxic T-lymphocyte associated antigen 4; Foxp3, forkhead box protein P3; GZMB, granzyme B; HES1, hairy and enhancer of split-1; ICOS, inducible T-cell co-stimulator; ID8agg-Luc, aggressive ID8 cells with luciferase expression; IFN-γ, interferon-gamma; IL10, interleukin-10; JAG2, jagged canonical notch ligand 2; MFI, mean fluorescent intensity; NICD1, notch1 intracellular domain; PD-1, programmed death 1; PNAd, peripheral node addressin; TCF-1, T cell transcription factor 1; Tex, exhausted T cells; Tex-int, intermediate-exhausted T cells; TLS, tertiary lymphoid structures; TNF-α, tumor necrosis factor-α; Tpex, progenitor-exhausted T cells; Treg, regulatory T cell.

cells. Our study provides a promising target for selectively inhibiting immune evasion mediated by TANs. Selective targeting of TANs represents an attractive strategy to overcome the immunosuppressive properties of the TME and to unleash immune effector cells to eradicate tumors. Recently, treatment of lung tumor-bearing mice with anti-JAG2 antibodies enhanced protective T cell immunity [52], suggesting that JAG2$^+$ TANs may serve as a potential target to restore protective immunity in tumors.

The modulation of Notch signaling could be a promising strategy for targeting immune cells in tumors, such as myeloid-derived suppressor cells [58]. Several antibodies that block the function of Notch receptors or ligands have already been developed [59, 60]. Notably, Notch signaling has been identified as a key determinant of response to ICI in small cell lung cancer [61]. Furthermore, the co-administration of an anti-PD-1 antibody with a Notch inhibitor significantly inhibited tumor growth in breast cancer models [62]. Our results indicate that the Notch inhibitor LY3039478 enhances the efficacy of anti-PD-1 antibody, supporting ongoing efforts to develop Notch inhibitors in combination with ICI therapy. Therefore, the combination of Notch inhibitors with ICIs could potentially sensitize tumors that are otherwise resistant to therapy when treated with an ICI alone.

Tregs have been implicated in the response to anti-PD-1 therapy [63], and therapeutic Treg depletion has been attempted in clinical trials [64]. A phase 1 dose-escalation trial of a third-generation anti-CD25 antibody, capable of selectively depleting Tregs without disrupting IL-2-STAT5 signaling in Teff cells, has recently commenced [65] Furthermore, a subsequent phase 1b study evaluating its combination with anti-PD-L1 therapy across multiple solid tumors is now underway (NCT04158583). These advances highlight the potential of Treg targeting approaches in combination with ICI as viable treatment strategies for patients with ovarian cancer. However, a significant concern with using anti-CD25 neutralizing antibodies is that they may indiscriminately target all Tregs, leading to generalized Treg cell depletion and potential systemic inflammation [66]. Therefore, strategies aimed at reducing the suppressive capacities or destabilizing Treg cells in the TME represent attractive targets for cancer immunotherapy. Our findings regarding the subset of eTregs that may play a critical role in therapy resistance further support this notion. eTreg cells are enriched in tumors, and their various immunological characteristics can be leveraged to modulate their functions. For instance, anti-CTLA4 antibodies primarily affect eTreg cells and reduce their suppressive activity [43, 67]. Additionally, as we have mentioned, strategies such as Notch signaling blockade and targeting JAG2$^+$ TANs to reprogram T cells could be valuable alternatives to merely targeting cell surface molecules.

TLS has been found in the stroma, invasive margins, or nests of different tumor types. TLS is not surrounded by fatty tissue and comprises a distinct T-cell zone, which is distinguished from the omental immune aggregates, "milky spots" [68, 69]. Notably, an increase in TLS was observed in tumors treated with a combination therapy of anti-PD-1 and LY3039478. This suggests that targeted inhibition of the Notch signaling pathway may enhance immune response to anti-PD-1 therapy in HGSOC. We also found that combination therapy led to increased infiltration of Tpex and Tex-int cells in tumors. Tpex cells typically appear in lymph nodes and TLS [70], indicating that their maintenance and differentiation, key components of activating adaptive immunity, are associated with the formation of TLS. The presence of TLS is linked to an improved prognosis and helps identify patients who are likely to benefit from immunotherapy [71, 72]. There remain several limitations in our findings. First, we did not provide experimental evidence to confirm the involvement of Blimp-1 in regulating eTreg gene expression. Further research is needed to determine which transcription factors RBPJ collaborates with to ensure the directed differentiation of eTregs. Additionally, although our findings indicate that JAG2 blockade reduces eTreg abundance in a murine HGSOC model, further validation in human HGSOC remains to be conducted. Importantly, although Notch inhibitors targeting Notch receptors and ligands have been clinically tested, factors such as dosing regimens and potential interactions between the two classes of inhibitors must be carefully considered when combining Notch inhibitors with checkpoint inhibitors.

5 | CONCLUSIONS

Our study revealed that JAG2$^+$ TANs create immunosuppressive TME by promoting the differentiation of eTreg cells through the JAG2/Notch1/RBPJ axis. Additionally, we observed that targeted inhibition of Notch signaling reprogrammed Treg cells. These findings also demonstrated that both the Notch inhibitor and anti-JAG2 antibody exhibited promising antitumor effects in xenograft models, suggesting a potential combination treatment regimen involving anti-PD-1 therapy for HGSOC with high JAG2$^+$ TAN infiltration.

AUTHOR CONTRIBUTIONS

Haiou Liu was responsible for the conceptualization and design of the study; Chenyang Wang and Moran Yang were responsible for the acquisition, analysis, and interpretation of data; Moran Yang, Yiying Wang, Kankan Cao, Mengdi He, Chen Zhang, Yujing Zhong and Xueling Wang provided technical support; Chenyang Wang and Haiou Liu

wrote the manuscript; Haiou Liu, Yan Huang, Guodong Zhang and Jiaqi Lu were responsible for the funding and supervision of the study. All authors read and approved the final manuscript.

ACKNOWLEDGMENTS

This work was supported by the Shanghai Key Laboratory of Female Reproductive Endocrine Related Diseases, the Obstetrics and Gynecology Hospital, Fudan University, and Shanghai Cancer Center, Fudan University.

CONFLICT OF INTEREST STATEMENT

The authors declare no potential conflicts of interest.

FUNDING INFORMATION

This study was funded by grants from the National Natural Science Foundation of China (82072881, 82273205, 82203665, 82473274), Natural Science Foundation of Shanghai (23ZR1408300), Shanghai Science and Technology Innovation Action Plan (23Y11909500, 23Y11901800), Shanghai Clinical Research Center for Gynecological Diseases (22MC1940200). All these study sponsors have no roles in the study design, in the collection, analysis and interpretation of data.

ETHICS APPROVAL AND CONSENT TO PARTICIPATE

The study was approved by the Ethics Committee of the Obstetrics and Gynecology Hospital of Fudan University (Kyy2016-49, Kyy2017-27) and the Ethics Committee of Shanghai Cancer Center (050432-4-2108*). The study was performed in accordance with the Declaration of Helsinki, and all patients provided written informed consent for sample collection and data analyses. Animal experiments were approved by the Ethics Committee of the Department of Laboratory Animal Science of Fudan University (2022JSFCKYY-063).

DATA AVAILABILITY STATEMENT

The bulk RNA-seq and corresponding clinical datasets were obtained from public paper [27], Array Express Archive (https://www.ebi.ac.uk/biostudies/arrayexpress) with the accession number: E-MATB-1733, the Gene Expression Omnibus (GEO) database under accession numbers GSE91061, GSE78220, GSE93157, GSE8841, GSE8842, GSE9899, GSE14764, GSE18520, GSE19829, GSE26712, GSE30161, GSE32063, GSE49997, and GSE51088 (https://www.ncbi.nlm.nih.gov/geo/), and the European Genome-phenome Archive under accession number EGAS0001002556 (https://ega-archive.org/). The scRNA-seq datasets analyzed in this study are publicly available in the GEO database under accession numbers GSE180661 and GSE137540. The raw data used in this study are available from the TCGA database (https://portal.gdc.cancer.gov/) under the TCGA-OV project. The corresponding author will provide all the data used in this study upon reasonable request.

ORCID

Chenyang Wang https://orcid.org/0009-0007-6895-4897
Haiou Liu https://orcid.org/0000-0003-0200-8981

REFERENCES

1. Hedrick CC, Malanchi I. Neutrophils in cancer: heterogeneous and multifaceted. Nat Rev Immunol. 2022;22(3):173–87.
2. Coffelt SB, Kersten K, Doornebal CW, Weiden J, Vrijland K, Hau C-S, et al. IL-17-producing γδ T cells and neutrophils conspire to promote breast cancer metastasis. Nature. 2015;522(7556):345–8.
3. Albrengues J, Shields MA, Ng D, Park CG, Ambrico A, Poindexter ME, et al. Neutrophil extracellular traps produced during inflammation awaken dormant cancer cells in mice. Science. 2018;361(6409):4227.
4. Ng MSF, Kwok I, Tan L, Shi C, Cerezo-Wallis D, Tan Y, et al. Deterministic reprogramming of neutrophils within tumors. Science. 2024;383(6679):6493.
5. Gungabeesoon J, Gort-Freitas NA, Kiss M, Bolli E, Messemaker M, Siwicki M, et al. A neutrophil response linked to tumor control in immunotherapy. Cell. 2023;186(7):1448–64.
6. Wu Y, Ma J, Yang X, Nan F, Zhang T, Ji S, et al. Neutrophil profiling illuminates anti-tumor antigen-presenting potency. Cell. 2024;187(6):1422–39.
7. Xue R, Zhang Q, Cao Q, Kong R, Xiang X, Liu H, et al. Liver tumour immune microenvironment subtypes and neutrophil heterogeneity. Nature. 2022;612(7938):141–7.
8. Wang L, Liu Y, Dai Y, Tang X, Yin T, Wang C, et al. Single-cell RNA-seq analysis reveals BHLHE40-driven pro-tumour neutrophils with hyperactivated glycolysis in pancreatic tumour microenvironment. Gut. 2023;72(5):958–71.
9. Fu H, Fu Z, Mao M, Si L, Bai J, Wang Q, et al. Prevalence and prognostic role of PD-L1 in patients with gynecological cancers: A systematic review and meta-analysis. Crit Rev Oncol Hematol. 2023;189:104084.
10. Cheng B-h, Liang H, Jiang T, Chen J-h, Wang G-H. Characterization of PD-L1 expression and its prognostic value in patients with ovarian cancer. Translational Cancer Res. 2018;7(5):1721–81.
11. Moore KN, Bookman M, Sehouli J, Miller A, Anderson C, Scambia G, et al. Atezolizumab, Bevacizumab, and Chemotherapy for Newly Diagnosed Stage III or IV Ovarian Cancer: Placebo-Controlled Randomized Phase III Trial (IMagyn050/GOG 3015/ENGOT-OV39). J Clin Oncol. 2021;39(17):1842–55.
12. Zhang Y, Chandra V, Riquelme Sanchez E, Dutta P, Quesada PR, Rakoski A, et al. Interleukin-17-induced neutrophil extracellular traps mediate resistance to checkpoint blockade in pancreatic cancer. J Exp Med. 2020;217(12):e20190354.
13. Kargl J, Zhu X, Zhang H, Yang GHY, Friesen TJ, Shipley M, et al. Neutrophil content predicts lymphocyte depletion and anti-PD1 treatment failure in NSCLC. JCI Insight. 2019;4(24):e130850.
14. Wang T-T, Zhao Y-L, Peng L-S, Chen N, Chen W, Lv Y-P, et al. Tumour-activated neutrophils in gastric cancer foster immune suppression and disease progression through GM-CSF-PD-L1 pathway. Gut. 2017;66(11):1900–11.

15. He G, Zhang H, Zhou J, Wang B, Chen Y, Kong Y, et al. Peritumoural neutrophils negatively regulate adaptive immunity via the PD-L1/PD-1 signalling pathway in hepatocellular carcinoma. J Exp Clin Cancer Res. 2015;34:141.
16. Linde IL, Prestwood TR, Qiu J, Pilarowski G, Linde MH, Zhang X, et al. Neutrophil-activating therapy for the treatment of cancer. Cancer Cell. 2023;41(2):356–72.
17. Yang M, Zhang G, Wang Y, He M, Xu Q, Lu J, et al. Tumour-associated neutrophils orchestrate intratumoural IL-8-driven immune evasion through Jagged2 activation in ovarian cancer. Br J Cancer. 2020;123(9):1404–16.
18. Radtke F, MacDonald HR, Tacchini-Cottier F. Regulation of innate and adaptive immunity by Notch. Nat Rev Immunol. 2013;13(6):427–37.
19. Amsen D, Helbig C, Backer RA. Notch in T Cell Differentiation: All Things Considered. Trends Immunol. 2015;36(12):802–14.
20. Tanaka A, Sakaguchi S. Regulatory T cells in cancer immunotherapy. Cell Res. 2017;27(1):109–18.
21. Dykema AG, Zhang J, Cheung LS, Connor S, Zhang B, Zeng Z, et al. Lung tumor-infiltrating Treg have divergent transcriptional profiles and function linked to checkpoint blockade response. Sci Immunol. 2023;8(87):1487.
22. Samon JB, Champhekar A, Minter LM, Telfer JC, Miele L, Fauq A, et al. Notch1 and TGFbeta1 cooperatively regulate Foxp3 expression and the maintenance of peripheral regulatory T cells. Blood. 2008;112(5):1813–21.
23. Cretney E, Xin A, Shi W, Minnich M, Masson F, Miasari M, et al. The transcription factors Blimp-1 and IRF4 jointly control the differentiation and function of effector regulatory T cells. Nat Immunol. 2011;12(4):304–11.
24. Neumann C, Heinrich F, Neumann K, Junghans V, Mashreghi M-F, Ahlers J, et al. Role of Blimp-1 in programing Th effector cells into IL-10 producers. J Exp Med. 2014;211(9):1807–19.
25. Cao K, Zhang G, Yang M, Wang Y, He M, Zhang C, et al. Attenuation of Sialylation Augments Antitumor Immunity and Improves Response to Immunotherapy in Ovarian Cancer. Cancer Res. 2023;83(13):2171–86.
26. Street K, Risso D, Fletcher RB, Das D, Ngai J, Yosef N, et al. Slingshot: cell lineage and pseudotime inference for single-cell transcriptomics. BMC Genomics. 2018;19(1):477.
27. Braun DA, Hou Y, Bakouny Z, Ficial M, Sant' Angelo M, Forman J, et al. Interplay of somatic alterations and immune infiltration modulates response to PD-1 blockade in advanced clear cell renal cell carcinoma. Nat Med. 2020;26(6):909–18.
28. Motzer RJ, Escudier B, McDermott DF, George S, Hammers HJ, Srinivas S, et al. Nivolumab versus Everolimus in Advanced Renal-Cell Carcinoma. N Engl J Med. 2015;373(19):1803–13.
29. Zilionis R, Engblom C, Pfirschke C, Savova V, Zemmour D, Saatcioglu HD, et al. Single-Cell Transcriptomics of Human and Mouse Lung Cancers Reveals Conserved Myeloid Populations across Individuals and Species. Immunity. 2019;50(5):1317–34.
30. Vázquez-García I, Uhlitz F, Ceglia N, Lim JLP, Wu M, Mohibullah N, et al. Ovarian cancer mutational processes drive site-specific immune evasion. Nature. 2022;612(7941):778–86.
31. Newman AM, Steen CB, Liu CL, Gentles AJ, Chaudhuri AA, Scherer F, et al. Determining cell type abundance and expression from bulk tissues with digital cytometry. Nat Biotechnol. 2019;37(7):773–82.
32. Magnuson AM, Kiner E, Ergun A, Park JS, Asinovski N, Ortiz-Lopez A, et al. Identification and validation of a tumor-infiltrating Treg transcriptional signature conserved across species and tumor types. Proc Natl Acad Sci U S A. 2018;115(45):E10672–E81.
33. Aibar S, González-Blas CB, Moerman T, Huynh-Thu VA, Imrichova H, Hulselmans G, et al. SCENIC: single-cell regulatory network inference and clustering. Nat Methods. 2017;14(11):1083–6.
34. Liu S, Wu W, Du Y, Yin H, Chen Q, Yu W, et al. The evolution and heterogeneity of neutrophils in cancers: origins, subsets, functions, orchestrations and clinical applications. Mol Cancer. 2023;22(1):148.
35. Ng LG, Ostuni R, Hidalgo A. Heterogeneity of neutrophils. Nat Rev Immunol. 2019;19(4):255–65.
36. Veglia F, Hashimoto A, Dweep H, Sanseviero E, De Leo A, Tcyganov E, et al. Analysis of classical neutrophils and polymorphonuclear myeloid-derived suppressor cells in cancer patients and tumor-bearing mice. J Exp Med. 2021;218(4):e20201803.
37. Jaillon S, Ponzetta A, Di Mitri D, Santoni A, Bonecchi R, Mantovani A. Neutrophil diversity and plasticity in tumour progression and therapy. Nat Rev Cancer. 2020;20(9):485–503.
38. Wang C, Zheng X, Zhang J, Jiang X, Wang J, Li Y, et al. CD300ld on neutrophils is required for tumour-driven immune suppression. Nature. 2023;621(7980):830–9.
39. Salcher S, Sturm G, Horvath L, Untergasser G, Kuempers C, Fotakis G, et al. High-resolution single-cell atlas reveals diversity and plasticity of tissue-resident neutrophils in non-small cell lung cancer. Cancer Cell. 2022;40(12):1503–20.
40. Stroud DA, Surgenor EE, Formosa LE, Reljic B, Frazier AE, Dibley MG, et al. Accessory subunits are integral for assembly and function of human mitochondrial complex I. Nature. 2016;538(7623):123–6.
41. Wing JB, Tanaka A, Sakaguchi S. Human FOXP3+ Regulatory T Cell Heterogeneity and Function in Autoimmunity and Cancer. Immunity. 2019;50(2):302–16.
42. Sainson RCA, Thotakura AK, Kosmac M, Borhis G, Parveen N, Kimber R, et al. An Antibody Targeting ICOS Increases Intratumoral Cytotoxic to Regulatory T-cell Ratio and Induces Tumor Regression. Cancer Immunol Res. 2020;8(12):1568–82.
43. Selby MJ, Engelhardt JJ, Quigley M, Henning KA, Chen T, Srinivasan M, et al. Anti-CTLA-4 antibodies of IgG2a isotype enhance antitumor activity through reduction of intratumoral regulatory T cells. Cancer Immunol Res. 2013;1(1):32–42.
44. van Hooren L, Handgraaf SM, Kloosterman DJ, Karimi E, van Mil LWHG, Gassama AA, et al. CD103+ regulatory T cells underlie resistance to radio-immunotherapy and impair CD8+ T cell activation in glioblastoma. Nat Cancer. 2023;4(5):665–81.
45. Li MO, Rudensky AY. T cell receptor signalling in the control of regulatory T cell differentiation and function. Nat Rev Immunol. 2016;16(4):220–33.
46. Di Giorgio E, Wang L, Xiong Y, Akimova T, Christensen LM, Han R, et al. MEF2D sustains activation of effector Foxp3+ Tregs during transplant survival and anticancer immunity. J Clin Invest. 2020;130(12):6242–60.
47. Chang J-H, Hu H, Jin J, Puebla-Osorio N, Xiao Y, Gilbert BE, et al. TRAF3 regulates the effector function of regulatory T cells and humoral immune responses. J Exp Med. 2014;211(1):137–51.
48. Munn DH, Sharma MD, Johnson TS. Treg Destabilization and Reprogramming: Implications for Cancer Immunotherapy. Cancer Res. 2018;78(18):5191–99.

49. Overacre-Delgoffe AE, Vignali DAA. Treg Fragility: A Prerequisite for Effective Antitumor Immunity? Cancer Immunol Res. 2018;6(8):882–7.
50. Browaeys R, Saelens W, Saeys Y. NicheNet: modeling intercellular communication by linking ligands to target genes. Nat Methods. 2020;17(2):159–62.
51. Bray SJ. Notch signalling: a simple pathway becomes complex. Nat Rev Mol Cell Biol. 2006;7(9):678–89.
52. Mandula JK, Sierra-Mondragon RA, Jimenez RV, Chang D, Mohamed E, Chang S, et al. Jagged2 targeting in lung cancer activates anti-tumor immunity via Notch-induced functional reprogramming of tumor-associated macrophages. Immunity. 2024;57(5):1124–40.
53. Liu Z, Zhang Y, Ma N, Yang Y, Ma Y, Wang F, et al. Progenitor-like exhausted SPRY1+CD8+ T cells potentiate responsiveness to neoadjuvant PD-1 blockade in esophageal squamous cell carcinoma. Cancer Cell. 2023;41(11):1852–70.
54. Chen Z, Ji Z, Ngiow SF, Manne S, Cai Z, Huang AC, et al. TCF-1-Centered Transcriptional Network Drives an Effector versus Exhausted CD8+T Cell-Fate Decision. Immunity. 2019;51(5):840–55.
55. Rahim MK, Okholm TLH, Jones KB, McCarthy EE, Liu CC, Yee JL, et al. Dynamic CD8+ T cell responses to cancer immunotherapy in human regional lymph nodes are disrupted in metastatic lymph nodes. Cell. 2023;186(6):1127–43.
56. Cabrita R, Lauss M, Sanna A, Donia M, Skaarup Larsen M, Mitra S, et al. Tertiary lymphoid structures improve immunotherapy and survival in melanoma. Nature. 2020;577(7791):561–5.
57. Liu Z, Brunskill E, Varnum-Finney B, Zhang C, Zhang A, Jay PY, et al. The intracellular domains of Notch1 and Notch2 are functionally equivalent during development and carcinogenesis. Development. 2015;142(14):2452–63.
58. Sierra RA, Trillo-Tinoco J, Mohamed E, Yu L, Achyut BR, Arbab A, et al. Anti-Jagged Immunotherapy Inhibits MDSCs and Overcomes Tumor-Induced Tolerance. Cancer Res. 2017;77(20):5628–38.
59. Ferrarotto R, Eckhardt G, Patnaik A, LoRusso P, Faoro L, Heymach JV, et al. A phase I dose-escalation and dose-expansion study of brontictuzumab in subjects with selected solid tumors. Ann Oncol. 2018;29(7):1561–8.
60. Cook N, Basu B, Smith D-M, Gopinathan A, Evans J, Steward WP, et al. A phase I trial of the γ-secretase inhibitor MK-0752 in combination with gemcitabine in patients with pancreatic ductal adenocarcinoma. Br J Cancer. 2018;118(6):793–801.
61. Roper N, Velez MJ, Chiappori A, Kim YS, Wei JS, Sindiri S, et al. Notch signaling and efficacy of PD-1/PD-L1 blockade in relapsed small cell lung cancer. Nat Commun. 2021;12(1):3880.
62. Meng J, Jiang Y-Z, Zhao S, Tao Y, Zhang T, Wang X, et al. Tumor-derived Jagged1 promotes cancer progression through immune evasion. Cell Rep. 2022;38(10):110492.
63. Kumagai S, Koyama S, Itahashi K, Tanegashima T, Lin Y-T, Togashi Y, et al. Lactic acid promotes PD-1 expression in regulatory T cells in highly glycolytic tumor microenvironments. Cancer Cell. 2022;40(2):201–18.
64. Vlahovic G, Archer GE, Reap E, Desjardins A, Peters KB, Randazzo D, et al. Phase I trial of combination of antitumor immunotherapy targeted against cytomegalovirus (CMV) plus regulatory T-cell inhibition in patients with newly-diagnosed glioblastoma multiforme (GBM). J Clin Oncol. 2016;34(15):e13518.
65. Solomon I, Amann M, Goubier A, Arce Vargas F, Zervas D, Qing C, et al. CD25-Treg-depleting antibodies preserving IL-2 signaling on effector T cells enhance effector activation and antitumor immunity. Nat Cancer. 2020;1(12):1153–66.
66. Yu SJ, Ma C, Heinrich B, Brown ZJ, Sandhu M, Zhang Q, et al. Targeting the crosstalk between cytokine-induced killer cells and myeloid-derived suppressor cells in hepatocellular carcinoma. J Hepatol. 2019;70(3):449–57.
67. Simpson TR, Li F, Montalvo-Ortiz W, Sepulveda MA, Bergerhoff K, Arce F, et al. Fc-dependent depletion of tumor-infiltrating regulatory T cells co-defines the efficacy of anti-CTLA-4 therapy against melanoma. J Exp Med. 2013;210(9):1695–710.
68. Meza-Perez S, Randall TD. Immunological Functions of the Omentum. Trends Immunol. 2017;38(7):526–36.
69. Rangel-Moreno J, Moyron-Quiroz JE, Carragher DM, Kusser K, Hartson L, Moquin A, et al. Omental milky spots develop in the absence of lymphoid tissue-inducer cells and support B and T cell responses to peritoneal antigens. Immunity. 2009;30(5):731–43.
70. Magen A, Hamon P, Fiaschi N, Soong BY, Park MD, Mattiuz R, et al. Intratumoral dendritic cell-CD4+ T helper cell niches enable CD8+ T cell differentiation following PD-1 blockade in hepatocellular carcinoma. Nat Med. 2023;29(6):1389–99.
71. Sautès-Fridman C, Petitprez F, Calderaro J, Fridman WH. Tertiary lymphoid structures in the era of cancer immunotherapy. Nat Rev Cancer. 2019;19(6):307–25.
72. Fridman WH, Meylan M, Petitprez F, Sun C-M, Italiano A, Sautès-Fridman C. B cells and tertiary lymphoid structures as determinants of tumour immune contexture and clinical outcome. Nat Rev Clin Oncol. 2022;19(7):441–57.

SUPPORTING INFORMATION

Additional supporting information can be found online in the Supporting Information section at the end of this article.

How to cite this article: Wang C, Yang M, Zhong Y, Cao K, Wang X, Zhang C, et al. Immunosuppressive JAG2^{+} tumor-associated neutrophils hamper PD-1 blockade response in ovarian cancer by mediating the differentiation of effector regulatory T cells. Cancer Commun.. 2025;1–27. https://doi.org/10.1002/cac2.70021